Spring 5-2015

Improved Monitoring of the Changjiang River Plume in the East China Sea During the Monsoon Season Using Satellite Borne L-Band Radiometers

Bumjun Kil
University of Southern Mississippi

The University of Southern Mississippi

IMPROVED MONITORING OF THE CHANGJIANG RIVER PLUME IN THE EAST CHINA SEA DURING THE MONSOON SEASON USING SATELLITE BORNE L-BAND RADIOMETERS

by

Bumjun Kil

Abstract of a Dissertation
Submitted to the Graduate School
of The University of Southern Mississippi
in Partial Fulfillment of the Requirements
for the Degree of Doctor of Philosophy

May 2015

ABSTRACT

IMPROVED MONITORING OF THE CHANGJIANG RIVER PLUME IN THE EAST CHINA SEA DURING THE MONSOON SEASON USING SATELLITE BORNE L-BAND RADIOMETERS

by Bumjun Kil

May 2015

Measurement of sea surface salinity (SSS) from Satellite borne L-band (1.4 GHz, 21cm) radiometers (NASA Aquarius/SAC-D and ESA SMOS) in the East China Sea (ECS) is challenging due to the uncertainty of SSS caused by land thermal emissions in the antenna side lobes and because of strong radio frequency interference (RFI) due to illegally emitted man-made sources. RFI contamination in the ECS has gradually decreased because of the on-going international efforts to eliminate broadcasts in the protected L-band radio-astronomy frequency band. The present dissertation focuses on carefully eliminating the remaining RFI contamination in retrieved SSS, and masking out regions close to the coast that are likely contaminated by thermal emissions from the land. Afterward, observation of SSS during the summer monsoon season in the ECS was conducted to demonstrate low salinity (< 28 psu) Changjiang Diluted Water (CDW) which is a mixture of Changjiang River (CR) plume mixing and the ambient ocean water causing ecosystem disruptions as far east as the Korean peninsula. In this study, during southeasterly wind, CDW was observed to be horizontally advected east-northeastward due to Ekman flow. In addition, monthly averaged Aquarius SSS presented one-month lagged robust relationship with freshwater flux. Despite limits on temporal information of SMOS, the detachment of CDW from its formation region and northeastward advection was successfully observed after the arrival of the tropical storm Matmo in the mainland China.

The University of Southern Mississippi

IMPROVED MONITORING OF THE CHANGJIANG RIVER PLUME IN THE EAST CHINA SEA DURING THE MONSOON SEASON USING SATELLITE BORNE L-BAND RADIOMETERS

by

Bumjun Kil

A Dissertation
Submitted to the Graduate School
of The University of Southern Mississippi
in Partial Fulfillment of the Requirements
for the Degree of Doctor of Philosophy

Approved:

Dr. Stephan Howden
Committee Chair

Mr. Robert Arnone

Dr. Dmitri Nechaev

Dr. Jerry Wiggert

Dr. Joel Wesson

Dr. Karen Coats
Dean of the Graduate School

May 2015

DEDICATION

To my god and my mother and my fiancée

ACKNOWLEDGMENT

I would like to thank Dr.Stephan Howden sincerely for leading and encouraging my life and graduate studies as my advisor. And I also would like to thank Mr. Robert Arnone, Dr. Dmitri Nechaev, and Dr. Jerry Wiggert of the DMS faculty and Dr. Joel Wesson in the Naval Research Laboratory for being my dissertation committee members. It has been my great pleasure to get much help from Dr. Derek Burrage and Dr. Joel Wesson at the Naval Research Laboratory since the beginning of this research project. And I would like to thank Dr.Ana Rice from the Naval Research Laboratory and Dr. Seunghyun Son from the National Oceanic and Atmospheric Administration for good reviewing and providing suggestions for the research. I would also like to thank the DMS faculty and staff and all my colleagues for their help. And I thank the Republic of Korea Navy for supporting my graduate study.

Thanks go out to the European Space Agency for providing the SMOS Level 2 Ocean Salinity data, which was downloaded by the Earth Observation Link (http: //earth.esa.int/EOLi/EOLi.html). The Aquarius/SAC-D data was provided by NASA Jet Propulsion Laboratory via Physical Oceanography Distributed Active Archive Center (http://podaac.jpl.nasa.gov/). The in situ salinity data was supplied by Republic of Korea National Fisheries Research and Development Institute by Korea Oceanographic Data Center at http://kodc.nfrdi.re.kr, and Korea Hydrographic and Oceanographic Administration via Korea Ocean Observing and Forecasting System at http://sms.khoa.go.kr/koofs. Thanks to NOAA, drifting buoy was acquired from AOML at http://www.aoml.noaa.gov/envids/index.php. The precipitation data used in this study were obtained as part of the mission of NASA's Earth Science Division and archived and distributed by the Goddard Earth Sciences (GES) Data and Information

Services Center (DISC) at http://daac.gsfc.nasa.gov/. WindSat data are produced by Remote Sensing Systems (RSS) and sponsored by the NASA Earth Science MEaSUREs (Making Earth Science Data Records for Use in Research Environments) DISCOVER Project and the NASA Earth Science Physical Oceanography Program. The RSS WindSat data was collected at www.remss.com. The ocean evaporation data was acquired from Objectively Analyzed Air-sea Fluxes (OAFlux) project available at http://oaflux.whoi.edu/. The outline of the Changjiang River Basin was provided by U.S. Geological Survey at http://hydrosheds.cr.usgs.gov.

TABLE OF CONTENTS

LIST OF TABLES

Table

LIST OF ILLUSTRATIONS

Figure

LIST OF ABBREVIATIONS

AOML	Atlantic Oceanographic and Meteorological Laboratory
CCC	Chinese Coastal Current
CDW	Changjiang Diluted Water
CR	Changjiang River
ECS	East China Sea
GLDAS	Global Land Data Assimilation System
GM	Geometric Mean
KC	Kuroshio Current
KODC	Korea Oceanography Data Center
LSW	Low Salinity Water
MIRAS	Microwave Imaging Radiometer with Aperture Synthesis
NFRDI	National Fisheries Research and Development Institute
NPO	Northwestern Pacific Ocean
OS	Ocean Salinity
RFI	Radio Frequency Interference
SCS	South China Sea
SMOS	Soil Moisture and Ocean Salinity
SSS	Sea Surface Salinity
T_b	Brightness Temperature
TGD	Three Gorges Dam
TRMM	Tropical Rainfall Measuring Mission

TWC	Taiwan Warm Current
YSWC	Yellow Sea Warm Current

CHAPTER I

INTRODUCTION

Study region and issue

The East China Sea (ECS) is one of the largest marginal seas extending from the southwestern area off Jeju (Cheju) Island to the northern area off Taiwan Island, and is bounded on the east by the Kuroshio and on the west by mainland China from which it receives the massive outflow from the Changjiang River (CR). Because of its large drainage basin, the CR contributes the majority of freshwater input to the coastal waters of China in the summer season (Mao et al., 1963; Beardsley et al., 1985; Delcroix & Murtugudde, 2002; Lie et al., 2003; Gimeno et al., 2012). The major currents in the ECS consist of the Taiwan Warm Current (TWC) which enters through Taiwan Strait toward the ECS from the South China Sea (e.g., Beardsley et al., 1985; Fang et al., 1991; Isobe, 1999), the Kuroshio Current (KC) which is a primary source of the Tsushima Current (TSC) , the Cheju (Jeju) Warm Current (CWC), and the Yellow Sea Warm Current (YSWC) (Figure 1) . The Chinese Coastal Current (CCC) flows southward along the Chinese coast (Beardsley et al., 1985).

The CR, one of the largest estuaries in the world (Beardsley et al., 1985), is an important freshwater source to the western Pacific Ocean (Chen et al., 1994). With an annually averaged discharge rate of 30×10^3 m^3/sec, and a maximum rate of 45×10^3 m^3/sec, 45% of the total freshwater flows out towards the northeast direction in the East China Sea forming a plume (Beardsley et al., 1985). Precipitation in the lower river basin also affects the amount of CR discharge with a one-month-time lag (Delcroix & Murtugudde, 2002). The Changjiang Diluted Water (CDW) is a mixture of CR discharged water with saline shelf water (Mao et al., 1963) having core

freshwater < 26 psu near the mouth of the river and more saline shelf water < 29 psu of sea surface salinity (SSS) (Beardsley et al., 1985; Lie et al., 2003; Moon et al., 2010). CDW is mainly transported southward by the coastal jet of the CCC (Beardsley et al., 1985), but in the summer season, it moves to Tsushima Strait through Jeju Island as a result of Ekman flow driven by constant southerly or southeasterly (north or northwestward) wind patterns and by tidal forcing (spring–neap tide cycle) near the Changjiang Bank which causes the CDW to expand (Beardsley et al., 1985) and detach from the river plume (Li & Rong, 2012; Moon et al., 2010; Moon et al., 2012; Wu et al., 2011; Xuan et al., 2012).

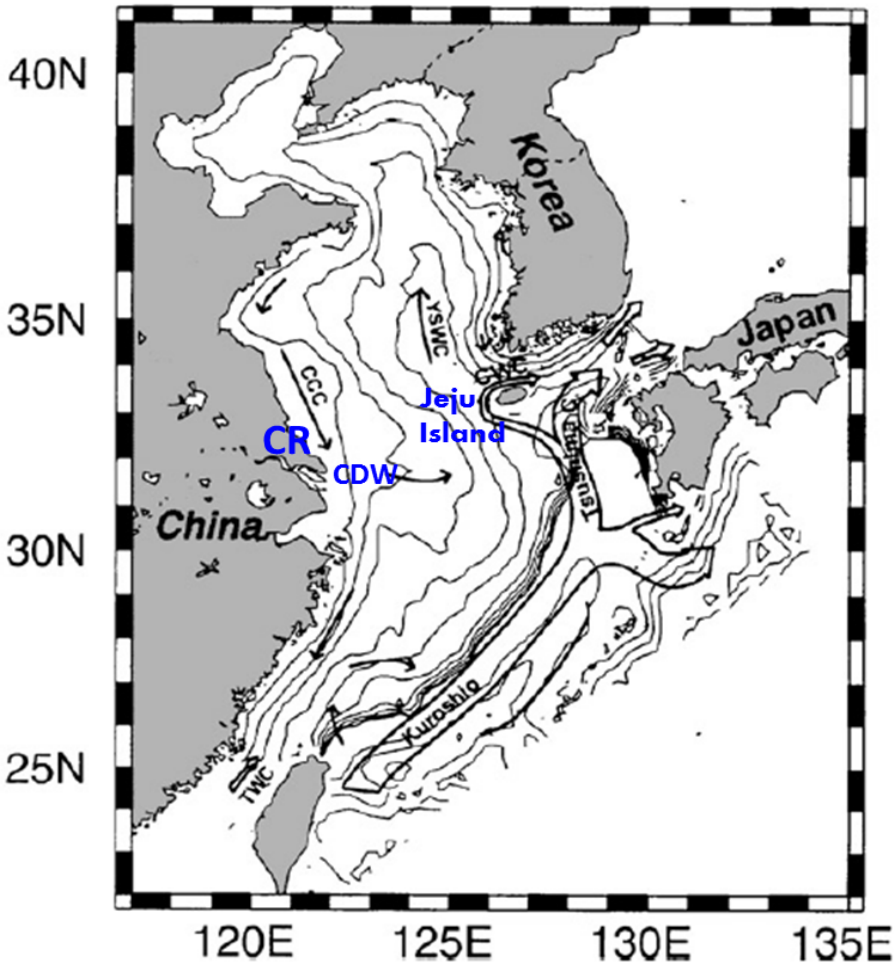

Figure 1. Schematic view of the circulation system in the summer monsoon season in the ECS (Image credit: Teague et al., 2003, Figure 10). CR, CDW and Jeju Island (see blue color) were marked for this dissertation.

During the summer season, the 10–15 m thick CDW is advected towards the northeast from the CR mouth to Jeju Island (Lie et al., 2003), as depicted by trajectories of drifting buoys (Figure 2a; Figure 3 in Chen et al., 2008). The path of typhoons toward the mainland China can bring strong southeasterly winds for a short period and can result in the expansion of CDW due to surface Ekman flow (Liu & Feng, 2012; Moon et al., 2012; Oh et al., 2014) (Figure 3).

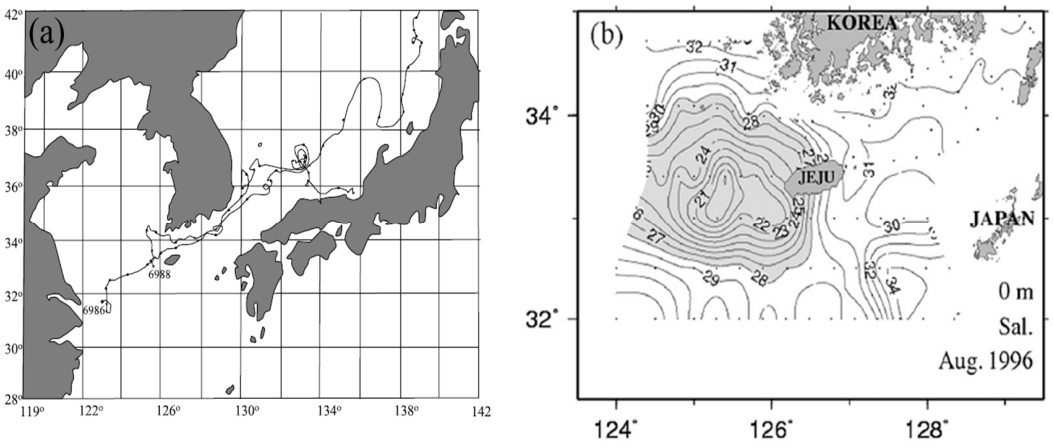

Figure 2. a) The trajectories of drifters (6986, 6988) released in summer 1986 (Image credit: Beardsley et al.,1992, Figure 4 and Chen et al., 2008, Figure 3), b) Horizontal distributions of surface salinity in August 1996 (Image credit: Suh et al.,1999, Figure 3 and Moon et al., 2010, Figure 1b).

During the summer season, the annual lowest salinity near the Jeju Island usually ranges from 28–32 psu with the exception of the advent of freshwater with salinity around 22 psu in 1996 (Figure 2b ; Suh et al., 1999). The watermass of unusually low salinity water (less than 28 psu) near the west coast of Jeju Island caused serious damage and economic losses in the fisheries industry in August, 1996 (Hyun & Pang, 1998; Suh et al., 1999; Lie et al., 2003; Moon et al., 2010). CDW is reported to be the main source of freshwater on the west coast of Jeju Island, advected by the ambient current in the summer season (Lie et al., 2003; Moon et al., 2009).

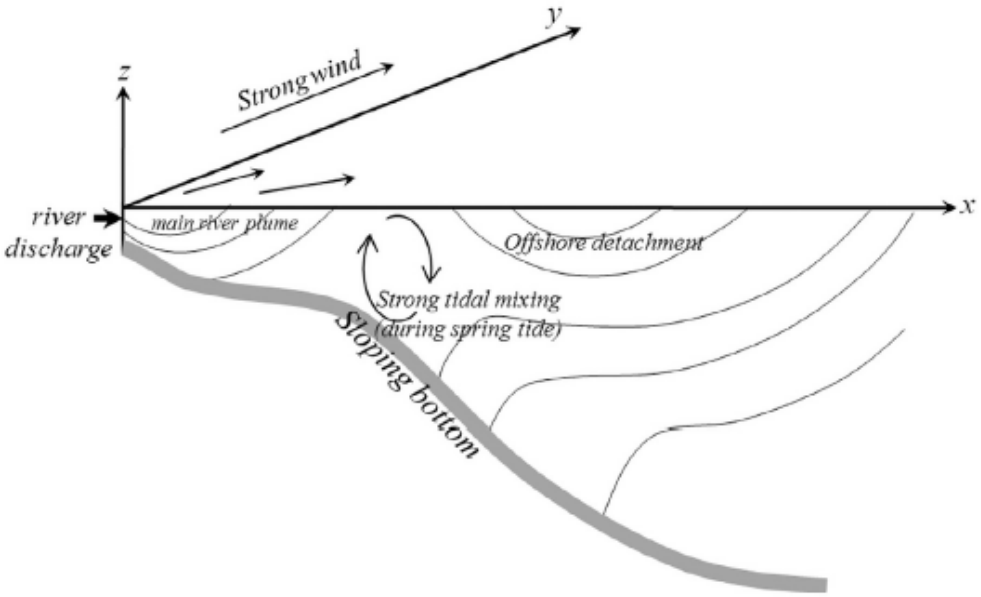

Figure 3. Schematic view of the detachment process of low-salinity water from the main CDW plume under conditions of Ekman transport and intense tide-induced vertical mixing near the mouth of the CR (Image credit: Moon et al., 2012, Figure 11), the offshore slope is about 200–250 km from the estuary with depth 30–50 meter (Moon et al., 2010; Moon et al., 2012).

While scientific efforts (e.g., numerical simulations, and cruise and deployment of drifting buoys) to prevent damage from future freshwater events are on-going, numerical prediction of the behavior of CDW is challenging because the characteristics of the CDW vary interannually (Moon et al., 2009). Within the CR estuary, the opposite problem is occurring: with the decreasing trend of river discharge since 1985 (An et al., 2009; Dai et al. 2008; Dai et al., 2011; Li et al., 2013) the risk of saltwater intrusion harming fisheries is increasingly becoming a problem. The increasing consumption of inland water and the completion of the Three Gorges Dam (TGD), located in the main stream of the Changjiang River, have both played a role in the decrease of river discharge (Dai et al. 2008; Dai et al. 2011; Gao et al., 2013; Xu & Milliman 2009). Furthermore, the reduction of river discharge due to the TGD, and the enormous amount of growing industrialization along the river are

known to have lead to toxic conditions in the CR at a sufficient level to elevate the risk of harmful algal blooms near the mouth of the river from increased domestic and industrial wastewater (Dai et al., 2011; Fu et al. 2010; Li et al., 2013). Although efforts are going on to monitor such ecosystem disruption using visible band satellite (e.g., MODIS, Landsat), retrieval of optical imagery near the mouth of CR is challenging due to frequent cloud covers during the monsoon season (Hu et al., 2010; Shen et al., 2012).

Sensing of sea surface salinity from spaceborne L-band radiometry

Presence of passive radiometer

Until 2010, with the exception of an experiment on the Skylab space station in the 1970's (Lerner & Hollinger,1977), SSS measurements from L-band (1.4 GHz, 21 cm, Figure 4) radiometers which use brightness temperature (T_b) emitted from the sea surface were only performed on aircraft. For example, measurements of SSS using the Salinity, Temperature and Roughness Remote Scanner (STARRS) have been conducted over Mobile Bay and Mississippi Sound (Wesson et al., 2008). This SSS sensed from passive microwave sea surface emissions has been compared with another SSS estimated from the optically-sensed Colored Dissolved Organic Matter (CDOM) in the Louisiana coastal waters (Maisonet et al., 2009; Wesson et al., 2008).

There are two spaceborne L-band radiometers. Aquarius/SAC-D satellite is operated by the joint U.S./Argentine Aquarius/Satélite de Aplicaciones Científicas (SAC)-D mission and was launched in June 2011 (Lagerloef et al., 2008). The instrument of the Aquarius/SAC-D (hereafter referred to as Aquarius) consists of a parabolic reflector with three feed horns which coincidently measure both passive radiometric signal to measure the SSS, and active scatterometric signal for measuring sea surface wind (roughness) from the same L-band (Le Vine et al., 2007; NASA JPL

PO.DAAC, 2014). From a three-beam system which correspond to incidence angles at 28.7°, 37.8°, 45.6°, SSS has an accuracy of 0.1–0.2 psu on global monthly averaged 150-km scales (Lagerloef et al., 2008; NASA JPL PO.DAAC, 2014) (Table 1 in Appendix A).

In November 2009, the European Space Agency (ESA) launched the Soil Moisture and Ocean Salinity (SMOS) satellite that carries the Microwave Imaging Radiometer with Aperture Synthesis (MIRAS) instrument, which provides 2-demensional image of Field of View (FOV) by interferometric Fourier synthesis from a Y-shaped antenna equipped with 69 receivers (Drinkwater, et al., 2009; Font et al., 2010a; Font et al., 2010b; Kerr et al., 2010; Pinori et al., 2008). Using the snapshot views from the FOV, MIRAS measures the SSS from the T_b at various incidence angles (0–55°) (Font et al., 2010a ; Kerr et al., 2000; Pinori et al., 2008; Zine et al., 2007). The spatial resolution of SMOS is about 40 km (Zine et al., 2008; Kerr et al., 2010). However, the initial oversampled pixels are based on the Icosahedron Snyder Equal Area (ISEA) grid spacing 15 km resolution (Boutin et al., 2012; Kerr et al., 2010; Reul et al., 2012). Its accuracy ranges about 1–2 psu for a single swath, depending on the position of the pixel within the field of view of the radiometer (Font et al., 2010b; Font et al., 2013). By spatial and temporal averaging over 10 days and 200×200 km, the inaccuracy can be reduced (Zine et al., 2007; Zine et al., 2008). For example, averaging the data over 100×100 km and 10 days enhances the accuracy to about 0.2 psu (Boutin et al., 2012; Boutin et al., 2013; Mecklenburg et al., 2012).

Aquarius and SMOS receive L-band radiation at the satellite antennas from the upper 2 cm of the water column, and thus the retrieved SSS is representatives of that over the same depth range. Since atmospheric absorption due to clouds and rain are small at the L-band (Burrage et al., 2002; Boutin et al., 2013; Ulaby et al., 1981;

Wentz, 2005), Aquarius and SMOS data are useful for cloudy and rainy summer monsoon season. While Aquarius has a higher level of accuracy of retrieved SSS, SMOS has better spatial and temporal resolution, with a wider swath width than Aquarius (Table 1 in Appendix A). More recently, in January 2015, NASA launched the Soil Moisture Active Passive (SMAP) mission which measures soil moisture using L-band radiometer with a wide swath range (1000 km), advanced spatial resolution (10 km) and more frequent revisit cycle (2–3 days) (Entekhabi et al. 2010; Entekhabi et al. 2014).

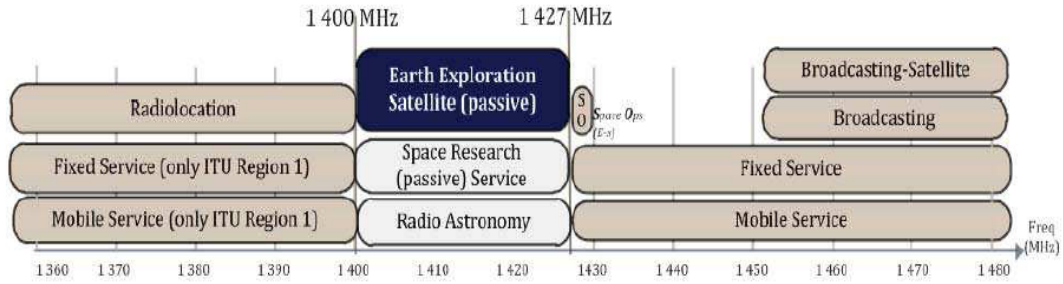

Figure 4. ITU-R frequency allocations in 1360–1480 MHz range and adjacent frequency bands (Image credit: Daganzo-Eusebio et al., 2013, Figure 1). 1400 - 1427 MHz is allocated for scientific purpose.

Because SMAP also collects the radiometric signal at the same L-band as Aquarius and SMOS (Entekhabi et al., 2010; Entekhabi et al., 2014), monitoring coastal SSS using SMAP is being developed by the NASA Jet Propulsion Laboratory (JPL) utilizing the techniques in noise reduction (see Challenges and effort section below) developed in the earlier missions (See document "Sea Surface Salinity Follow-on Data" at http://smap.jpl. nasa.gov).

SSS from L-band radiometry

Gustav Robert Kirchhoff (1824–1887) stated in the 1860s that "at thermal equilibrium, the power radiated by an object must be equal to the power absorbed." This leads to the observation that if an object absorbs 100 percent of the radiation

incident upon it it must re-radiate 100 percent (Riedl, 2001) under equilibrium conditions. However, most radiation sources are not black bodies (opaque materials that absorb all the incident radiation from all directions at all frequencies; Figure 5). Some of the energy incident upon them may be reflected or transmitted. The ratio of the radiant emittance (W') of such a source and the radiant emittance (W) of a blackbody at the same temperature is called the emissivity ( ) of the source :

—

With this relation, different types of radiation sources can be classified as indicated in Figure 5, where the curve for the blackbody with = 1 is Plank's curve. The curve for gray bodies (i.e., real materials) do not emit as much energy as black bodies do at the same temperature. The ratio is also equal to the ratio of brightness temperature ( ) for particular incidence angle ( ) and polarization (*p*) ( ) to physical temperature (T_{ph} : sea surface temperature (SST)), thus can be defined as following.

———

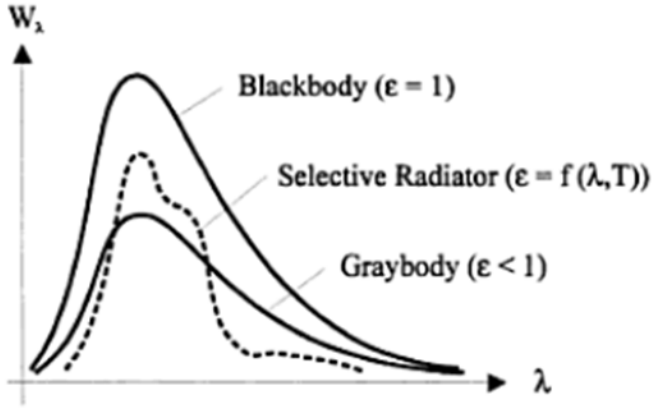

Figure 5. Spectral radiant emittance of three types of radiators (Image credit: Riedl, 2001, Figure 1.5).

Since L-band T_b has been known for some time as an important parameter for measuring SSS (Droppleman et al., 1970; Lerner & Hollinger,1977), algorithms were developed for airborne and space measurement of SSS via Tb and ancillary measurements (Klein & Swift, 1977; Swift & McIntosh, 1983) as following:

Assuming the ocean fills a flat half–space and is in thermal equilibrium, $e_p(\theta)$ is calculated from measured (T_b) as equation 2 (here, T_b is a function of particular incidence angle, polarization, SST and SSS ($T_{b\ flat,p}(\theta, SST, SSS)$). Then Fresnel power reflection coefficient at single polarization ($R_p(\theta)$) from $e_p(\theta)$ (Swift & McIntosh, 1983) is estimated as follows:

$$e_p(\theta) = 1 - R_p(\theta) \qquad (4)$$

For a surface plane, the Fresnel coefficient (R) is dependent on the incident angle θ and the complex dielectric constant of seawater, □:

$$R_H = \left| \frac{cos\theta - \sqrt{\varepsilon - sin^2\theta}}{cos\theta + \sqrt{\varepsilon - sin^2\theta}} \right| \qquad (5)$$

$$R_V = \left| \frac{\varepsilon\ cos\theta - \sqrt{\varepsilon - sin^2\theta}}{\varepsilon\ cos\theta + \sqrt{\varepsilon - sin^2\theta}} \right| \qquad (6)$$

Because $e(\theta)$ has an important connection to estimate dielectric constant () which depends on the concentration of salt in the sea water (Swift & McIntosh, 1983), ionic conductivity (σ) can be estimated within the microwave band using the Debye's expression (Debye, 1929):

$$\varepsilon = \varepsilon_\infty + \frac{(\varepsilon_s - \varepsilon_\infty)}{1 + i\omega\tau} - i\frac{\sigma}{\omega\varepsilon_0} \qquad (7)$$

Here, several auxiliary parameters are required to estimate σ. $\omega = 2\pi f$ is the radian frequency with f in Hz, i is the imaginary number, ε_∞ is the electric permittivity at an infinite frequency, ε_s is the static dielectric constant; τ is the relaxation time and ε_0 is a constant called the permittivity of free space. ε_s, τ and σ are dependent on the temperature and salinity of seawater (Klein & Swift, 1977). By using SST, σ can be estimated sinceε_0, ε_∞, ε_s and τ have been empirically determined for seawater (Klein & Swift, 1977). Using this algorithm, salinity can be estimated in units of psu (practical salinity units, UNESCO, 1981).

However, the actual T_b of the sea surface includes a portion due to sea surface roughness as following:

$$T_{b,p}(\theta, SST, SSS, U_{10}) = T_{b\,flat,p}(\theta, SST, SSS) + \Delta T_{b\,rough,p}(\theta, U_{10}) \qquad (3)$$

Here $T_{b,p}(\theta, SST, SSS, U_{10})$ is measured T_b which consists of T_b on flat surface ($T_{b\,flat,p}(\theta, SST, SSS)$),and increment T_b due to sea surface roughness ($\Delta T_{b\,rough,p}(\theta, U_{10})$). $\Delta T_{b\,rough,p}$ is necessary for preventing the bias of T_b due to sea surface roughness. In addition to the wind speed at 10 meter above the sea surface (U_{10}) and θ, $\Delta T_{b\,rough,p}$ can be estimated depending on additional parameters (e.g., wind direction, significant wave height etc.).

In terms of satellite applications, Aquarius corrects $\Delta T_{b\,rough,p}$ using wind speed coincidently measured by an L-band scatterometer on the satellite, and employs National Centers for Environmental Prediction (NCEP) optimum interpolation (OI) sea surface temperature (SST) (bulk temperature) for use in the dielectric model that is used in the inversion for SSS (NASA JPL PO.DAAC, 2014). On the other hand, SMOS employs predicted SST and roughness parameters (significant wave height, wind speed and direction) from the European Centre for Medium-Range Weather

Forecasts (ECMWF) model with three different kinds of roughness correction algorithms with various range of wind speed (See Table 2 in Appendix A).

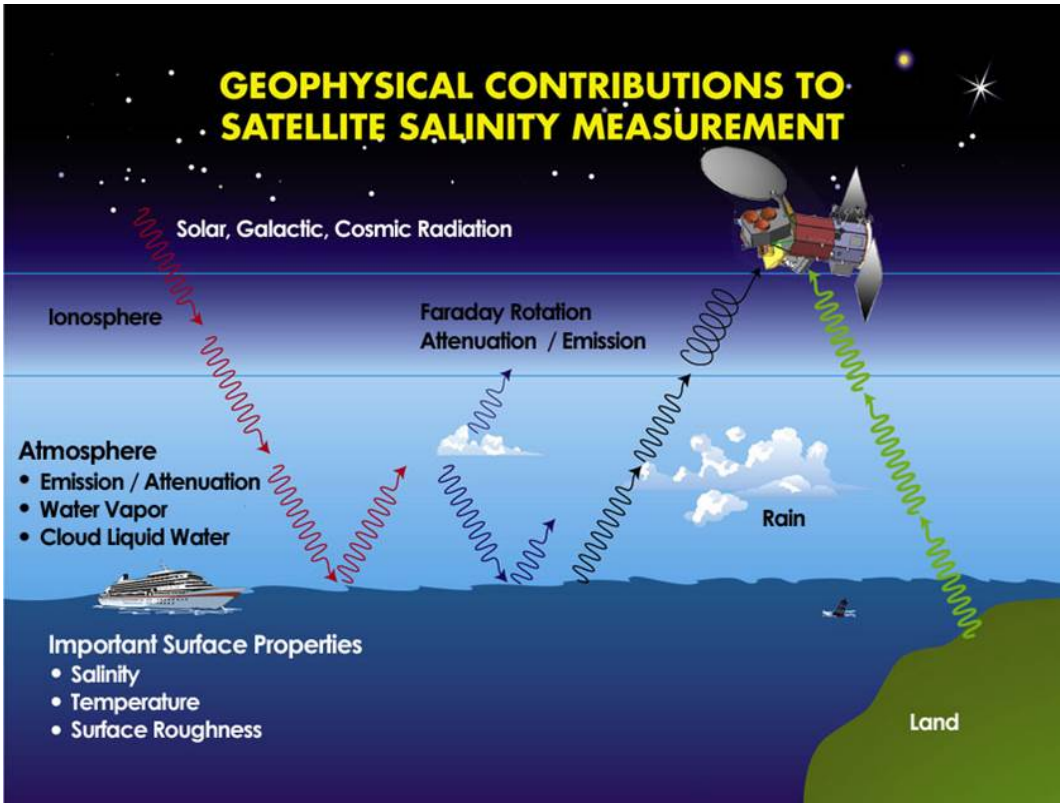

Figure 6. Originations influencing passive microwave remote sensing (Image credit: NASA Aquarius web, http://aquarius.nasa.gov/)

In addition to the roughness effect, T_b also can be affected by the emission from space sources (e.g., moon, sun and galaxy etc.; Le vine et al., 2014a; Kerr et al., 2010; Figure 6). Thus, Aquarius and SMOS include data quality flags for use in reducing contaminated SSS (See Table 3, 4 in Appendix A).

The products from the L-band radiometers go through multiple layers of processing (NASA JPL PO.DAAC, 2014; SMOS TEAM, 2008). In general terms, Level 0 are data in engineering units, the highest Level 1 products are the georeferenced T_b measurements along the satellite swaths, Level 2 products give the georeferenced T_b inverted to SSS, and Level 3 are gridded products. In producing Level 3 data, choices have to be made on which data to utilize in the gridding process.

In order to develop new procedures for using data flags to select "good" data for gridding in the particular region or under particular condition, Level 2 is the highest processed data type that can be worked with.

Studies using L-band radiometer in the river outflowing area

Monitoring the SSS surrounding a river mouth with L-band radiometry remote sensing provides a means to track the development of river plumes as they flow into the coastal ocean. Using Aquarius and SMOS, Grodsky et al. (2012) studied the effects of salinity stratification in the Amazon and Orinoco river plumes for strengthening tropical storms. Fournier et al. (2012) analyzed the temporal coherence between SSS and CDOM in the river plume in the tropical Atlantic Ocean. Gierach et al. (2013) studied the variational impact of Mississippi River discharge into the Gulf of Mexico using Aquarius and SMOS SSS. For the same region, Kil et al. (2014) studied the offshore advection of Mississippi River plume in the center of Gulf of Mexico after tropical cyclone Isaac made landfall by inferring SMOS SSS with optically estimated CDOM.

Challenges and effort

A challenge to the measurement of SSS in the coastal area is the impact of Radio Frequency Interference (RFI), emitted from man-made sources, on the measurement of T_b (Font et al., 2010a; Font et al., 2010b; Mecklenburg et al., 2012; Oliva et al., 2012; Reul et al., 2012). When the footprint of the antenna on the spacecraft is close to RFI sources (mostly on land) the T_b appears to be much higher than usual (Aksoky et al., 2013; Oliva et al., 2012). Europe and Asia are known as regions where RFI emission is very strong (Daganzo-Eusebio et al., 2013; Oliva et al., 2012) (Figure 7).

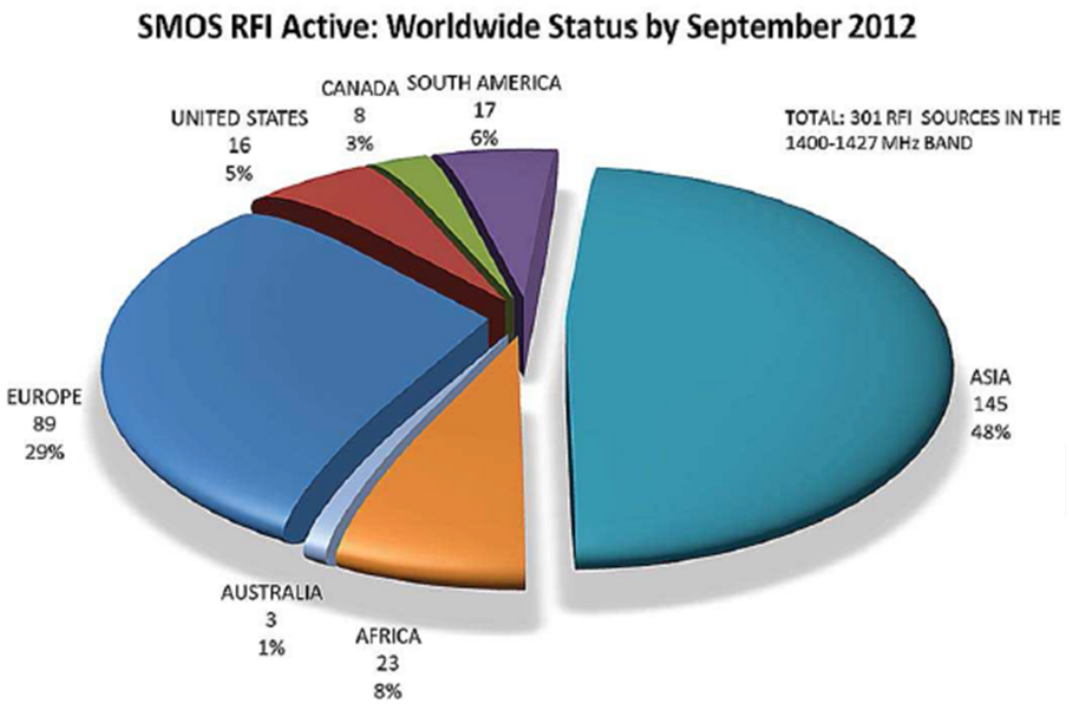

Figure 7. Distribution of active RFI sources worldwide as of September 2012 (Image credit: Daganzo-Eusebio et al., 2013, Figure 8)

A study in a coastal area in the South Atlantic Ocean pointed out that SMOS captures not only the mesoscale but also possibly the small-scale movement of low salinity water near the mouth of a river better than Aquarius because of its high spatial and temporal resolution (Guerrero et al., 2014; Hernandez et al., 2014).

Because the portion of the L-band used for SSS remote sensing is a radiofrequency protected band for astronomy, transmissions in that part of the band are restricted by international agreement (Kerr et al., 2010; Oliva et al., 2012). SSS remote sensing uses a passive radiometer to observe the sea surface, but there are many illegal man-made transmissions in the protected band. An international effort to "switch off" the illegal man-made noise is on-going and has successfully reduced the RFI sources (Daganzo-Eusebio et al., 2013; Font et al., 2013; Mecklenburg et al., 2012; Oliva et al., 2012; Oliva et al., 2014).

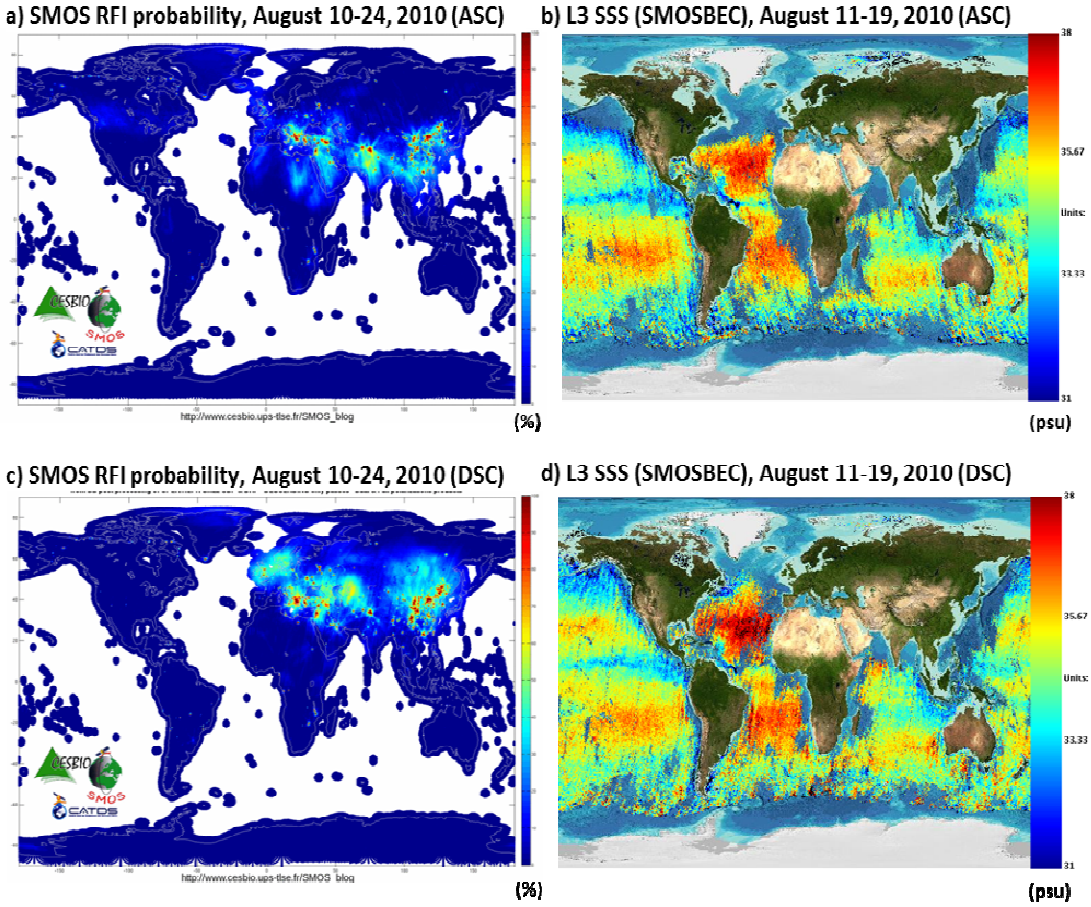

Figure 8. Global RFI distribution for a) ascending and c) descending passes during August 10–24, 2010 (Image credit: Cesbio, http://www.cesbio.ups-tlse.fr/SMOS_blog/), Global map of monthly averaged SSS of b) ascending pass and d) descending pass in August, 2010 (Image credit: SMOS BEC, http://www.smos-bec.icm.csic.es/). SSS in the East Asian region is not presented mostly due to RFI contamination.

In the ECS (and in other regions, including Europe) the SMOS Level-3 product is not available because the measurements are flagged as contaminated by RFI (Figure 8). Aquarius SSS is also known to have a negative bias, as does SMOS in the same regions, due to low-level RFI (Aksoy et al., 2013; Lagerloef et al., 2013). Addtionally, because the T_b of land is much higher than for the ocean, a large bias in T_b (i.e., negative bias in SSS) occurs when the major axis of field of view (FOV) approaches within ~100 km from the coast (Burrage et al., 2002; Zine et al., 2007).

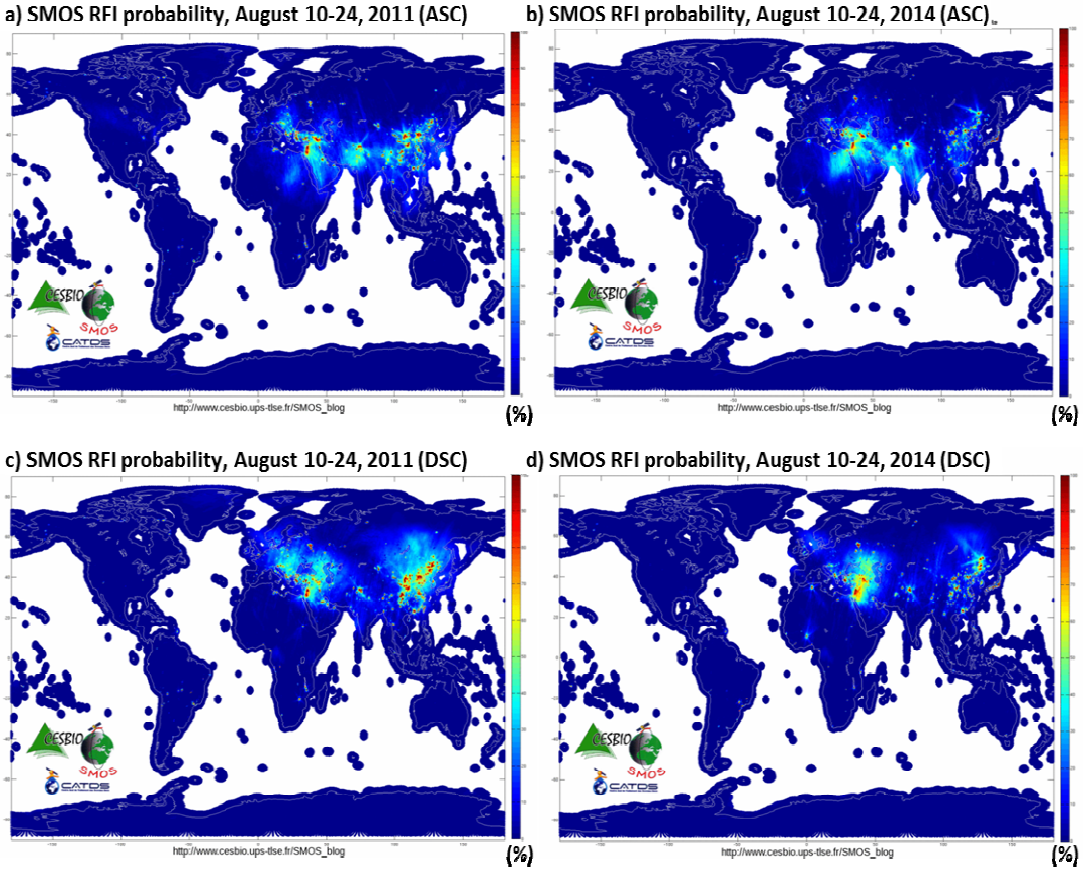

Figure 9. Global RFI distribution in a, c) August 10–24, 2011 and b, d) August 10–24, 2014 for a, b) ascending and c, d) descending passes (Image credit: Cesbio, http://www.cesbio.ups-tlse.fr/SMOS_blog/). The RFI sources (size of bright to red shading) appear considerably decreased in 2014.

Thus, processing T_b data from both Aquarius and SMOS near coastal areas requires care because of both RFI and strong land emission around the main and the side lobes of the antennae (Kerr et al., 2010; Lagerloef et al., 2013). As a result of the international effort to mitigate RFI, the impact of RFI globally has been diminishing since 2010 (Daganzo-Eusebio et al., 2013; Font et al., 2013; Mecklenburg et al., 2012; Oliva et al., 2012; Oliva et al., 2014). As shown in Figure 9, the RFI sources in 2014 are considerably reduced as compared with 2010 (Figure 8) and 2011 for both ascending and descending passes. Even though strong RFI sources are still present in the ECS, the trend of steady elimination of RFI sources has reduced the impact of measuring T_b over the ocean.

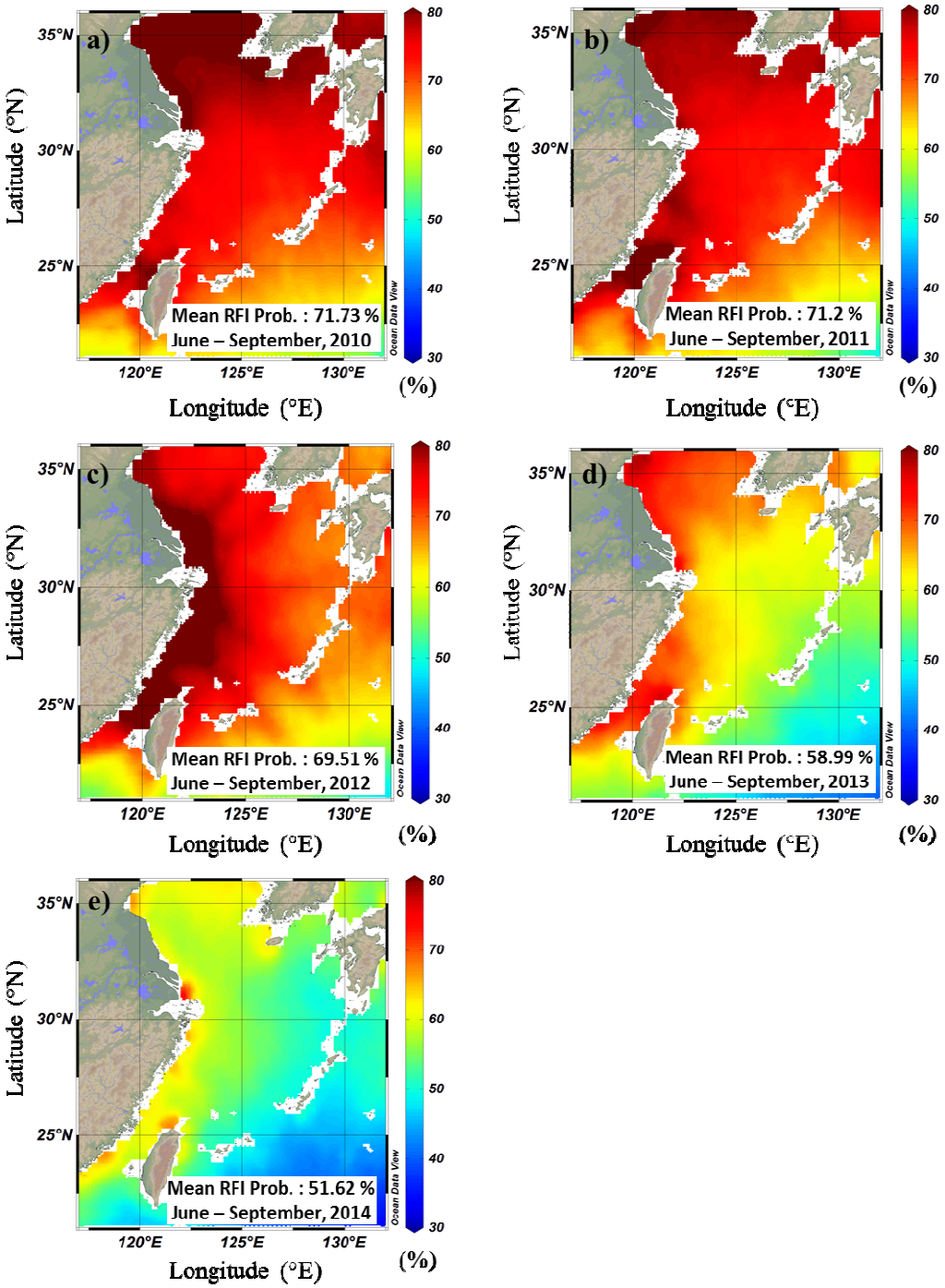

Figure 10. Annual RFI probability distribution of SMOS in the ECS during each monsoon season (June–September) from 2010 to 2014.

This is illustrated in Figure 10, where RFI probability was estimated from the SMOS Level-2 ocean salinity (OS) product (Appendix A) based on the number of measured T_b that deviated exceedingly from the modeled T_b for all incidence angles

(SMOS TEAM, 2008). Over the time period shown in Figure 10, the mean RFI probability has decreased considerably from 71.73% in 2010, to 69.51% in 2012, to 58.99 % in 2013, and down even more to 51.62% in 2014. In addition, the region of intensive RFI contamination (see the red shadings in the Figure 10) retreated towards the coast by 2013, probably because of the on-going international effort to protect the L-band radio-astronomy frequency band. Consequently, because of the deceased mean RFI probability in the ECS, SSS from both Aquarius and SMOS may be able to capture low salinity water during the monsoon season in the ECS.

Using the L2 Aquarius product, Kim et al.(2014) retrieved SSS in the ECS during a period of diminished RFI contamination and found that the ascending passes of Aquarius avoided RFI contamination more than the descending passes. Moreover, selecting pixels at least 150 km from the coast reduced the radiometric land fraction to < 0.5 % (Kim et al., 2014).

However, the current version of Aquarius L3 product (version 3), has been considerably improved in flags and calibration from previous versions (e.g., correction of long term drift and high frequency “wiggles” in the radiometer signals, flagging RFI contamination using RFI filtered (TF) minus unfiltered antenna temperature (TA), and correcting small SST-dependent errors; see details at ftp://podaac-ftp.jpl.nasa.gov/allData/aquarius/docs/v3/Aquarius_V3.0V2.0_ SummaryOfChanges.pdf). Thus, in the present dissertation, version 3 of Aquarius level-3 (L3: Globally mapped data from the L2 swath) SSS in the ECS was examined to determine how well salinity features in the ECS can be detected and studied despite land and RFI contamination of T_b.

Unlike Aquarius, which has three real aperture antennae, SMOS has a 2-dimensional interferometric antenna which measures T_b from various incidence

angles (0–55°) using 69 elementary antennas (Kerr et al., 2010). The differences in the systems give them different susceptibilities to contamination from RFI and land thermal emissions, and Aquarius appears to be less susceptible (Le Vine et al., 2014b). There are numerous SMOS L2 flags that can be utilized to reduce noise and contamination (See Table 4 in Appendix A), and algorithms can be selected depending on the sea surface roughness correction model (See Table 2 in Appendix A). In the ECS, because of numerous RFI sources, few numbers of measurements are available if all of the flags are used as recommended by ESA (Figure 8).

The current trend of reduction of RFI sources may likely contribute to improvements of SMOS SSS, even though the measurements are flagged as contaminated by RFI. Ren et al. (2015) examined temporal averaged (7 days averaged; 0.05°×0.05°) SMOS level-2 SSS in the South China Sea (SCS). They suggested SMOS L2 SSS is usable in the SCS since RFI sources are far from the land, and temporal averaging and the combination of ascending and descending reduces the uncertainty of SSS (Ren et al., 2015).

Hypothesis and Objectives

Since the RFI probability in the ECS has gradually decreased, the success of using SMOS data from the SCS may indicate that SMOS can provide usable SSS data in the ECS. In this dissertation, new procedures are therefore developed for using the ESA RFI flags to see if enough SMOS L2 SSS data can be retrieved during the summer monsoon season over the ECS.

Because RFI sources in the ECS are being reduced as a result of international efforts, the null hypothesis is established as:

Sea surface salinity retrievals from satellite-borne L-band radiometers cannot be improved enough to detect lower salinity surface water in the East China Sea because of the RFI contamination in the region.

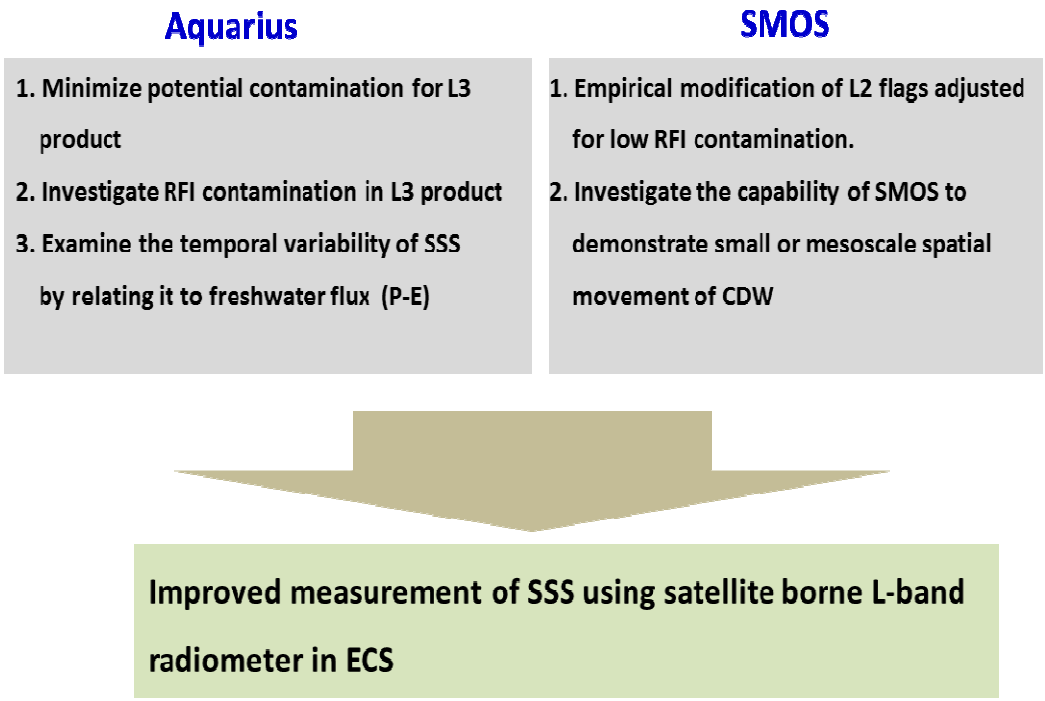

Figure 11. Objective map of the present dissertation

The overarching goal of the present dissertation is to improve SSS retrievals from satellite-borne L-band radiometers in the ECS. The objectives are divided between Aquarius and SMOS processing tasks, for improving the measurement of SSS using satellite-borne L-band radiometers in ECS, as outlined in Figure 11.

Aquarius Level 3 (version 3) only uses Level 2 product data that is not flagged as having severe land and RFI contamination (See Table 3 in Appendix A; NASA JPL PO.DAAC, 2014). The Level 3 data will be carefully sampled in the ECS to meet the following objectives: □ Minimize potential RFI and land contamination in the Level 3 product, □ Investigate the bias of independent passes from in situ SSS and select the applicable pass, and □ Examine the relationship between Aquarius SSS over the ECS

and freshwater flux (precipitation minus evaporation, P-E) which is averaged over the CR basin and over a region in the ECS.

SMOS will be used for capturing the small or mesoscale spatial variability in the ECS. Because the SMOS L3 product rarely covers the ECS, even with the reduction in RFI sources, due to the globally applied threshold (Chuprin and Font, 2012; SMOS TEAM, 2008, see Table 4 of Appendix A), Level 2 SSS will be analyzed after careful removal of RFI contaminated measurements by developing an empirical procedure for using the flags in the ECS region. Thus, the objectives of SMOS data processing are: □ Developing the new procedure for utilizing the Level 2 data quality flags that allows more uncontaminated SSS data to be used; and □ Through the higher spatial and temporal resolution of SMOS demonstrating the ability to detect spatial features of low salinity CDW water within the ECS. The data will be selected at times when the RFI probability is small (i.e., the flag that indicates that there is a high probability of RFI contamination is small). Then, selected SMOS SSS data will be compared with L3 Aquarius SSS data to check the similarity of SSS from the two instruments.

APPENDIX A

RFI probability in the ocean (Fraction of RFI measurements to the grid point in SMOS L2 OS product) (Chuprin & Font, 2012; SMOS TEAM, 2008)

$$= 100 \times \frac{Dg\_RFI\_L2}{Dg\_num\_meas\_l1c}$$

Dg_RFI_L2: Number of RFI outlier measurements

Dg_num_meas_l1c: Number of measurement available in L1C product

Description of Aquarius/SAC-D and SMOS satellites (Lagerloef et al., 2008; Kerr et al., 2010)

	Aquarius/SAC-D	SMOS
1. Launch	June, 2011	November, 2009
2. Revisit cycle	7 days	3 days
3. Spatial resolution	150 km	35 km (Oversampling:15 km)
4. Incidence angle	28.7°, 37.8°, 45.6°	0° - 55°
5. Accuracy (Monthly)	0.1–0.2 psu	~ 0.2 psu (100×100 km)
6. Width of the swath	390 km	1050 km

Comparison of roughness correction algorithms between Aquarius and SMOS

	Aquarius	SMOS		
		Alg.1	Alg.2	Alg.3
1. Roughness sources	Observed wind (Scatterometer in Aquarius)	Predicted wind (ECMWF)		
2. Correcting method	Geophysical Model Functions for radar backscatter cross section (Meissner et al., 2014)	Two-scale electromagnetic model (Durden and Vesecky, 1985; Yueh, 1997; Johnson & Zhang, 1999; Dinnat et al., 2003) + Foam model (Yin et al.,2012)	Small slope approximation and Kudryavtsev wave spectrum model (Irisov, 1997; Kudryavtsev et al., 1999; Johnson & Zhang, 1999) + Foam model (Reul & Chapron, 2003)	Semi-empirical Model (Camps et al., 2004; Gabarró et al., 2004)
3. Applicable range of wind speed (m/sec)	3 - 15 m/sec (Meissner et al., 2014)	3 – 12 m/sec (Boutin et al., 2012)	2 – 15 m/sec (Boutin et al., 2012)	3 – 10 m/sec (Boutin et al., 2012)

Aquarius (version 3) flags for L3 processing (NASA JPL PO.DAAC, 2014)

Flag name	Description	Flag classification
1. Flag 3	Land contamination	Radiometric land fraction > 1% (Severe)
2. Flag 4	Sea ice contamination	Radiometric land fraction > 1% (Severe)
3. Flag 5	High wind speeds	Radiometer HH-pol Wind Speed > 20 m/sec (Severe)
4. Flag 18	Cold SST	SST < 0 °C (Severe)
5. Flag 19	Unusual brightness temperature (RFI filtered (TF) minus unfiltered (TA) antenna temperatures)	T-TA difference (Severe) TF – TA < -1.00 or TF – TA > 0.30
6. Flag 21	Moon contamination (Reflected radiation from Moon)	Rad_moon_Ta_ref_I > 0.5 (Severe)
	Galaxy contamination (Reflected radiation from Galaxy)	Rad_galact_Ta_ref_I > 5.6K or Rad_galact_Ta_ref_I > 3.6K and HH wind < 3 m/sec

SMOS (version 550) L2 flags (Chuprin and Font, 2012; SMOS TEAM, 2008)

Flag name	Description	Classification
1. Fg_ctrl_many_outlier	Too many outlier measurements for a grid	Measurement is outlier if abs($T_b$model[pol] – $T_b$smos [pol]) > 5× rad_noise
2. Fg_ctrl_suspect_rfi	Flag set if the number of RFI (T_b outliers) larger than the threshold (RFI probability)	RFI Probability = 33%
3. Fg_ctrl_chi2_P	Poor fit quality from test on chi2 (Flag set for the outside of acceptability probability)	$0.05 \leq$ Chi2_P ≤ 0.95
4. Fg_ctrl_range	Retrieved SSS (Acard) is the outside range	$0 <$ SSS < 42
5. Fg_ctrl_range_Acard	Retrieved Cardioid model (Acard) is the outside range	$30 <$ Acard < 65
6. Fg_ctrl_sigma	Retrieved σSSS exceeds the threshold	$\sigma SSS \leq 5$
7. Fg_ctrl_sigma_Acard	Retrieved σAcard exceeds the threshold	$\sigma Acard \leq 5$
8. Fg_ctrl_reach_maxiter	Maximum number of iteration reached before convergence	Threshold = 20
9. Fg_ctrl_marq	Iteration stopped due to Marquardt increment too big	Threshold = 100
10. Fg_ctrl_sunglint	Flag for high sun glint above threshold	Tg_sunglint_max = 10%

(continued).

Flag name	Description	Flagging classification
11. Fg_ctrl_moonglint	Flag for moon specular reflection above threshold	Tg_moonglint_max = 10%
12. Fg_ctrl_gal_noise	Flag set if grid point has too many measurements flagged as contaminated by galactic noise	Tg_gal_noise_max = 10%
13. Fg_ctrl_num_meas_low	Processed, but with a low number of measurements.	Tg_num_meas_valid = 30
14. Fg_ctrl_retriev_fail	Flag raised if iterative scheme returns an error	Processing error
15. Fg_sc_high_wind, Fg_sc_low_wind	Acceptable ranges of wind speed (WS)	$3 \leq WS \leq 12$ m/sec
16. Fg_sc_high_sst Fg_sc_low_sst	Acceptable ranges of SST	$10 \leq SST \leq 25$ °C
17. Fg_sc_high_sss Fg_sc_low_sss	Acceptable ranges of SSS	$31 \leq SSS \leq 37$ psu
18. Fg_sc_TEC_gradient	Threshold of high Total electron count (TEC) gradient along dwell for a grid point	5000 Tecu
19. Fg_sc_suspect_ice	Suspect ice on grid point	Tg_suspect_ice = 50%
20. Fg_sc_rain	Heavy rain suspected at grid point as defined by ECMWF rain rate	Tg_max_rainfall= 10mm/h
21. Fg_sc_land_sea_coast	Flags set by the distance from the coast	40, 100, 200 km from the coast

CHAPTER II

ANALYSIS OF AQUARIUS SSS

Method and Materials

Aquarius L3 SSS version 3 bias-adjusted product (file format ends with "SSS_bias_adjusted") from August 2011 to December 2014 (Table 1) was downloaded from the Physical Oceanography Distributed Active Archive Center (PODAAC; ftp://podaac-ftp.jpl.nasa.gov/allData/aquarius/). Even though the L3 product discards L2 data with land and RFI contamination flags set at values indicating severe contamination (Flag 3 : Land fraction in L2 product : > 1 %, Flag 19 : RFI filtered (TF)–unfiltered antenna temperature (TA) < -1.0 K or > 0.3 K), the data near the coast are still potentially contaminated. Kim et al. (2014) recommended only using data from ascending passes with land fraction < 0.5 % in the ECS, which is mostly that data at least 150 km from the coast. In this dissertation, only those Aquarius L3 data which were at least 150 km from the coast were used. The region selected for utilizing the L3 data is shown in Figure 12a and will be referred to as AQL3ECS. This contains 24 gridpoints of the L3 product. The coordinates of the region are shown in Table 1 in Appendix B (see the red polygon in the Figure 12a). The L3 SSS data selected in AQL3ECS for the period of July 5–9, 2014 had, relative to the the entire ECS, land fraction reduced by 0.31 % for ascending passes, 0.32 % for descending passes, and 0.32 % for combined ascending and descending passes, (Table 2; Figure 13 b , d, f).

Using the SSS in AQL3ECS, the differences between ascending and descending passes were estimated using monthly averaged SSS. RFI probability in the SMOS L2 ocean product was used to check the impact of RFI on this difference.

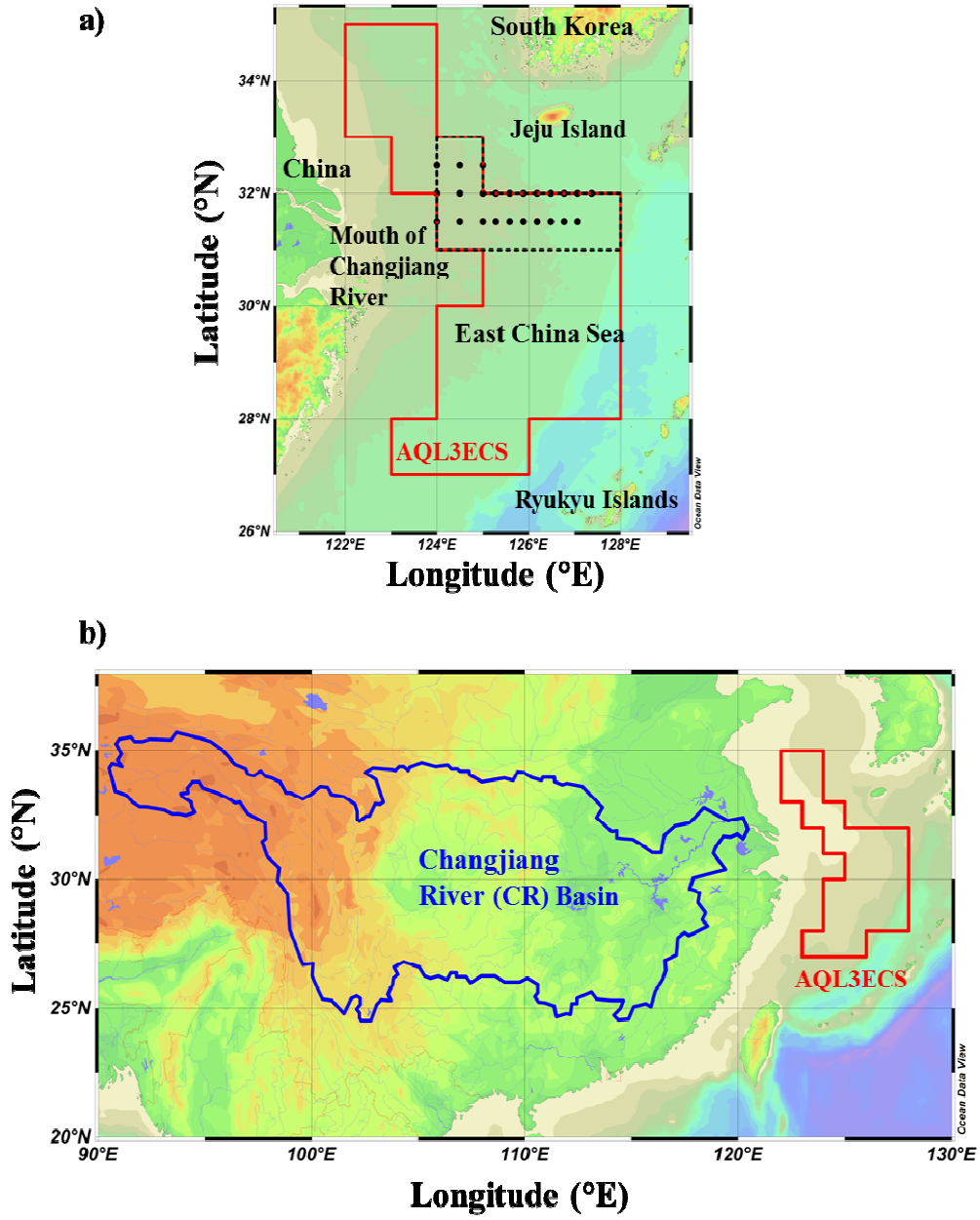

Figure 12. a) Area for Aquarius experiment (red polygon represents the L3 collecting area of Aquarius SSS; the black dashed polygon is the area for estimating the mean of $SSS_{AQL3ECS}$ minus SSS_{insitu}). b) Area for estimating P-E for CR Basin (blue polygon, data source : http://hydrosheds.cr.usgs.gov/index.php) and AQL3ECS (red polygon).

In situ data from annual cruise measurements from November 2011 to August 2014, collected by the National Fisheries Research and Development Institute (NFRDI), were employed for estimating the bias of the Aquarius 7 days SSS (The data is retrievable from the Korea Oceanography Data Center (KODC) at http://kodc.

nfrdi.re.kr). The comparison was conducted by estimating the difference for spatially-averaged SSS by the region outlined in the black dashed lined box in Figure 12a).

Table 1

Dataset for Aquarius experiments

Instrument	Data	Mission	Dates	Purpose
1. Remote sensing	SSS (Bias adjusted)	Aquarius	August, 2011 – December, 2014	L2 : Surveying land fraction (July 5-9, 2014) L3: Comparing with P-E
	Rain rate	TRMM (L3/3B43)	August, 2011 - September, 2014	Estimating P-E
2. In situ data	SSS	KODC	November,2011 –August, 2014	Comparing $SSS_{in\ situ}$ with $SSS_{AQL3ECS}$
3. Auxiliary data	Evaporation	GLDAS	August, 2011 - September, 2014	Estimating P-E at CR basin (Land)
		OAflux	August, 2011 - September, 2014	Estimating P-E at Area2 (Ocean)

The temporal variability of Aquarius SSS in AQL3ECS (here we denote this data as $SSS_{AQL3ECS}$) was investigated by relating the data with freshwater sources from the river and atmosphere. It is difficult to acquire direct river discharge data for the CR. However, it can be estimated by integrating precipitation (P) minus

evaporation (E) over the river basin. P-E for the CR basin is most important near the river mouth for discharge (Baumgartner & Reichel, 1975;Dai & Trenberth, 2002). The freshwater flux over the CR Basin can be estimated by monthly precipitation minus evaporation, where we use $P_{CR\ Basin}$ -$E_{CR\ Basin}$ (Ferreira et al., 2013). Here, $P_{CR\ Basin}$ and $E_{CR\ Basin}$ are the areal integrated value (mm/month) by averaging over the regional outline of CR Basin (see blue polygon at Figure 12b) implemented by Ferreira et al., (2013) (Appendix B). For the ocean, monthly freshwater flux was integrated over the outline of AQL3ECS region ($P_{AQL3ECS}$- $E_{AQL3ECS}$) as same approach with $P_{CR\ Basin}$ -$E_{CR\ Basin}$. Hereinafter the subscripts are dropped on P for clarity (i.e., P-$E_{CR\ Basin}$ and P- $E_{AQL3ECS}$).

In order to estimate monthly P-$E_{CR\ Basin}$ and P- $E_{AQL3ECS}$ during the period of August, 2011 to September, 2014, monthly precipitation data from the Tropical Rainfall Measuring Mission (TRMM;3B43) was downloaded from Goddard Earth Sciences Data and Information Services Center (GES DISC) (http://disc.sci.gsfc. nasa.gov/). For the CR basin, simulated evaporation rates estimated by the Common Land Model (CLM, Dai et al., 2003; Rodell et al., 2007), stored in the Global Land Data Assimilation System (GLDAS) (same link as TRMM data), was used. For the ocean, evaporation rates over the AQL3ECS region ($E_{AQL3ECS}$) was downloaded from the Objectively Analyzed air-sea Flux (OAFlux) project by Woods Hole Oceanographic Institution (WHOI) (http://oaflux. whoi.edu/evap.html) which applies the evaporation equation by Yu et al. (2008).

Finally, the statistical significance of the linear relation between $SSS_{AQL3ECS}$ versus P-$E_{CR\ Basin}$ and P-$E_{AQL3ECS}$ was tested using the t-test *P-value* (Appendix B).

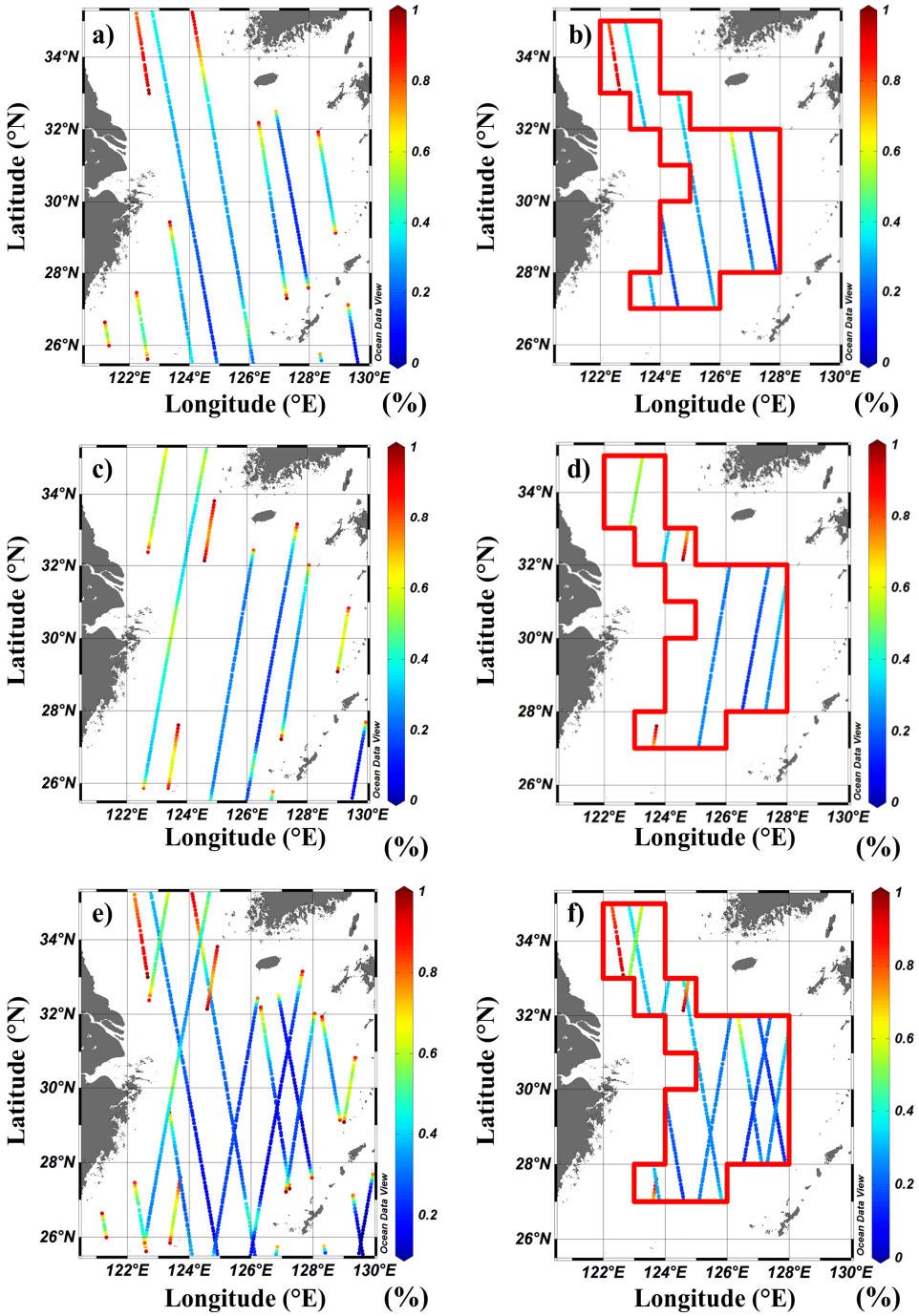

Figure 13. Aquarius filtered land fraction (< 1 %) using Flag 3 in the ECS on July 5–9, 2014 for a) ascending c) descending e) ascending+descending passes. Land fraction (< 1 %) in AQL3ECS is shown in b) ascending d) descending f) ascending+ descending passes.

Table 2

Mean land fraction of Aquarius in the ECS. AQL3ECS collects L3 SSS, which applies Flag 3.

	ASC (%)	DSC (%)	A+D (%)	Reference (%)
1. Total swath in ECS	5.81	4.88	5.35	
2. Application of Flag 3	0.37	0.38	0.38	0.5 (Kim et al.,2014)
3. AQL3ECS	0.31	0.32	0.32	

Results and discussion

Temporal differences between ascending (ASC) and descending (DSC) passes

In order to investigate the temporal variation of $SSS_{AQL3ECS\ (DSC\ minus\ ASC)}$, we collected Aquarius monthly L3 SSS data from August 2011 to November 2014. At the beginning of the mission, the differences between DSC and ASC passes were greater than 1 psu (negative $SSS_{AQL3ECS\ (DSC\ minus\ ASC)} < -1$ psu), with particularly large differences in April and May of 2012. With the exception of February of 2012, the differences were less than 1 psu ($SSS_{AQL3ECS\ (DSC\ minus\ ASC)} > -1$ psu). The large negative $SSS_{AQL3ECS\ (DSC\ minus\ ASC)}$ might have been due to RFI, which is not properly filtered in the L3 processing. From May 2013, the standard deviation of the monthly data decreased and in 2014 the $SSS_{AQL3ECS\ (DSC\ minus\ ASC)}$ had an overall trend towards zero (Figure 14; Table 3). This could be a result of the decrease in RFI sources.

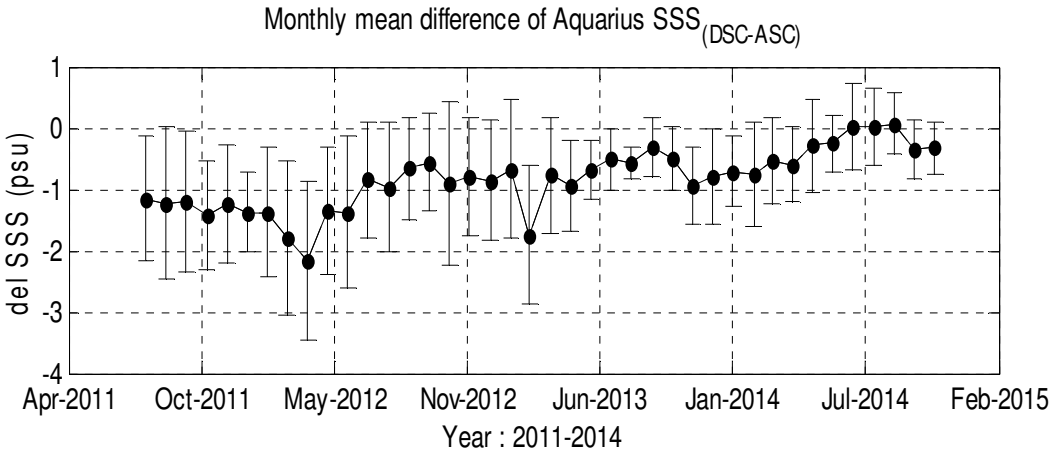

Figure 14. Monthly mean of Aquarius SSS (descending–ascending passes) from 2011 to 2014 in AQL3ECS.

Table 3

Annual difference of the $SSS_{AQL3ECS}$ between ascending and descending pass (2011-2014)

		Dec., 2011 –Nov., 2012	Dec., 2012 –Nov., 2013	Dec., 2013 -Nov., 2014
1. $\Delta SSS_{AQL3ECS}$ (descending -ascending passes)	Mean difference (psu)	-1.22	-0.77	-0.38
	STD (psu)	1.13	0.83	0.69
	N	267	264	265
2. RFI Probability (%)		75.3	68.86	59.3

The DSC data are known to be very sensitive to RFI because the Aquarius antennae sidelobes are directed more towards strong RFI sources during the spacecraft's overflight (Kim et al., 2014). The negative $SSS_{AQL3ECS\ (DSC\ minus\ ASC)}$ indicates that the DSC passes are likely more contaminated by RFI, which increases the T_b measured and lowers the retrieved SSS. This strong negative bias of DSC passes is shown in the mean difference between Aquarius 7 days SSS and in situ SSS during 2011–2014 for south of Jeju Island (Figure. 14).

The ASC pass data is closer to the in situ SSS than is the DSC pass data for all years (Figure 15). The bias of ASC passes was significantly lower than previously reported when SMOS RFI probability was decreased by < 70% and shows a positive bias by August of 2014 (Table 4). For instance, $SSS_{(ASC\text{-}Insitu)}$ averaged over the period of November 2013 to August 2014, was -0.07 psu (Figure 15). This is an improvement over a similar comparison by Kim et al. (2014) that showed a -0.4 psu bias for the period of October 2011 and of -0.93 psu for the period of September, 2011. Since the Aquarius SSS data from ASC passes showed little bias from in situ SSS, in contrast to DSC passes, the ASC data were selected for comparison with the P-E data. The trend in the reduction of DSC SSS bias may eventually allow those data to be used in future comparisons, but for the purposes of this dissertation the data from the DSC passes were not used.

Relationship between SSS and P-E

In general, discharge of a river lags behind the integrated P-E over its watershed. Delcroix and Murtugudde (2002) found that CR outflow lagged behind precipitation. The time lag relation between monthly averaged $SSS_{AQL3ECS}$ and $P - E_{CRbains}$ was investigated by estimating their lagged correlation coefficients (i.e., the correlation function). As shown in Figure 16, increasing trend of $P\text{-}E_{CRBasin}$ during the

Table 4

Annual mean difference between $SSS_{AQL3ECS}$ and $SSS_{In\ situ}$ from 2011 to 2014 (see black dashed polygon in Figure 12a)

Year	Month	$SSS_{(ASC\text{-}Insitu)}$ (psu)	$SSS_{(DSC\text{-}Insitu)}$ (psu)	$SSS_{(AD\text{-}Insitu)}$ (psu)	RFI Probability (%)
2011	Nov.	-0.46	-1.78	-1.07	75.44
2012	Feb.	-1.19	-3.1	-1.96	76.73
	May.	-0.6	-3.59	-1.67	75.68
	Aug.	-0.41	-0.96	-0.81	73.4
	Nov.	-0.39	-2.03	-0.85	74.65
2013	Jan.	-0.96	-1.82	-1.19	77.95
	May	0.2	-0.67	-0.28	69.41
	Aug.	0	-0.01	-0.02	62.28
	Nov.	-0.17	-1.72	-0.94	66.03
2014	Feb.	-0.71	-1.16	-0.78	65.19
	Apr.	0.02	-0.56	-0.28	56.55
	Aug.	0.57	0.97	0.71	52.03
Reference (Kim et al., 2014)		-0.4 (Oct., 2011), -0.93 (Sept., 2011)			

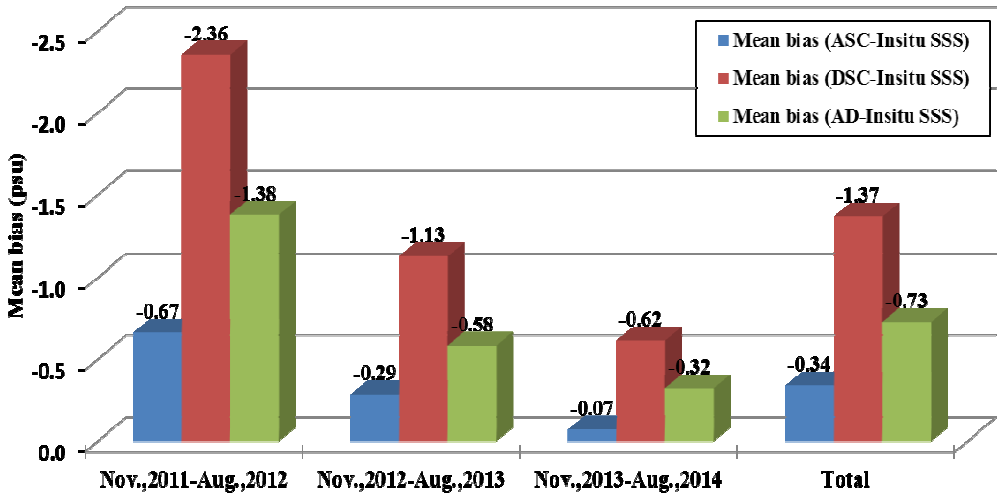

Figure 15. Histogram of bias of 7 day averaged Aquarius SSS from SSS_{Insitu} (2011-2014)

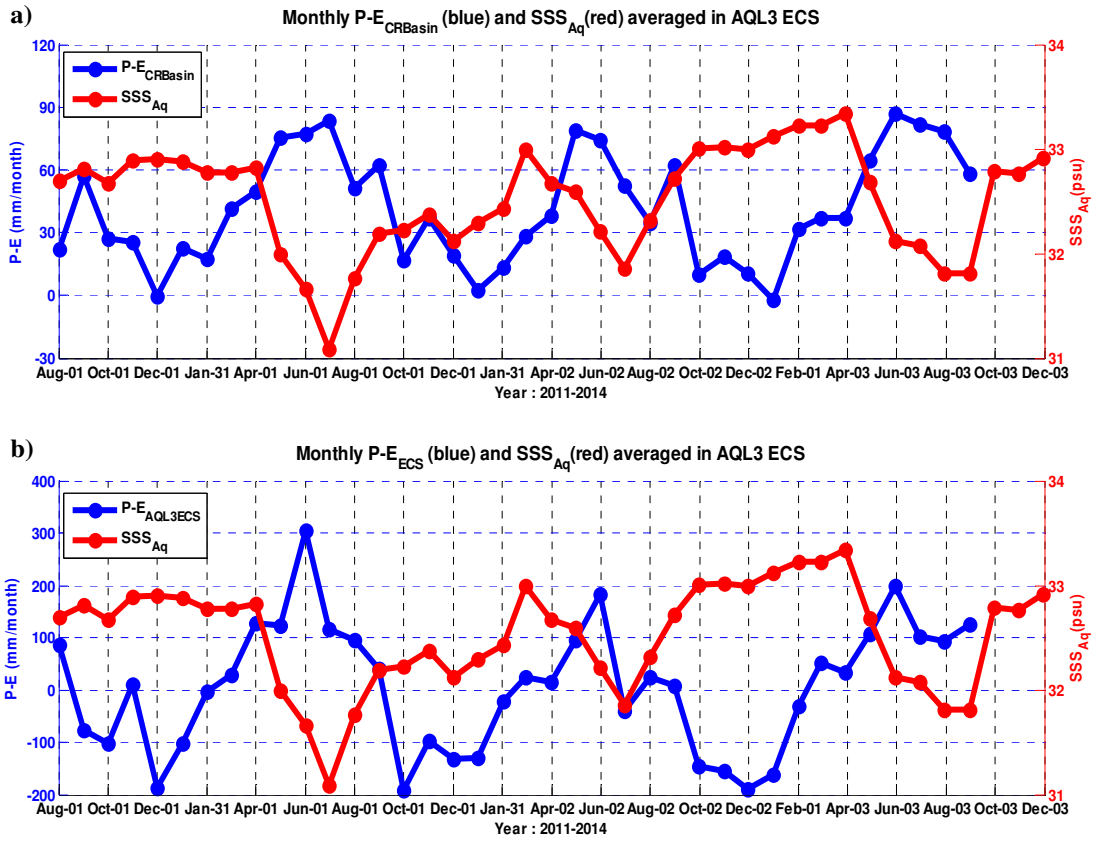

Figure 16. Monthly time series of $SSS_{AQL3ECS}$ (red line) with a) $P\text{-}E_{CR\ basin}$, b) $P\text{-}E_{AQL3ECS}$ (blue line).

summer monsoon season leads decreasing $SSS_{AQL3ECS}$. $P\text{-}E_{AQL3ECS}$ shows a peak in the time of elevated $P\text{-}E_{CRBasin}$ as well. In addition, $SSS_{AQL3ECS}$ has statistical significance (*P-value* < 0.05) with both $P\text{-}E_{CRBasin}$ and $P\text{-}E_{AQL3ECS}$ (Figure 17a, b). The robust relationship (*P-value* < 0.001, the correlation coefficient: -0.58) found between $P\text{-}E_{CRBasin}$ and $SSS_{AQL3ECS}$ indicates that the temporal variability of SSS is likely affected by the river runoff.

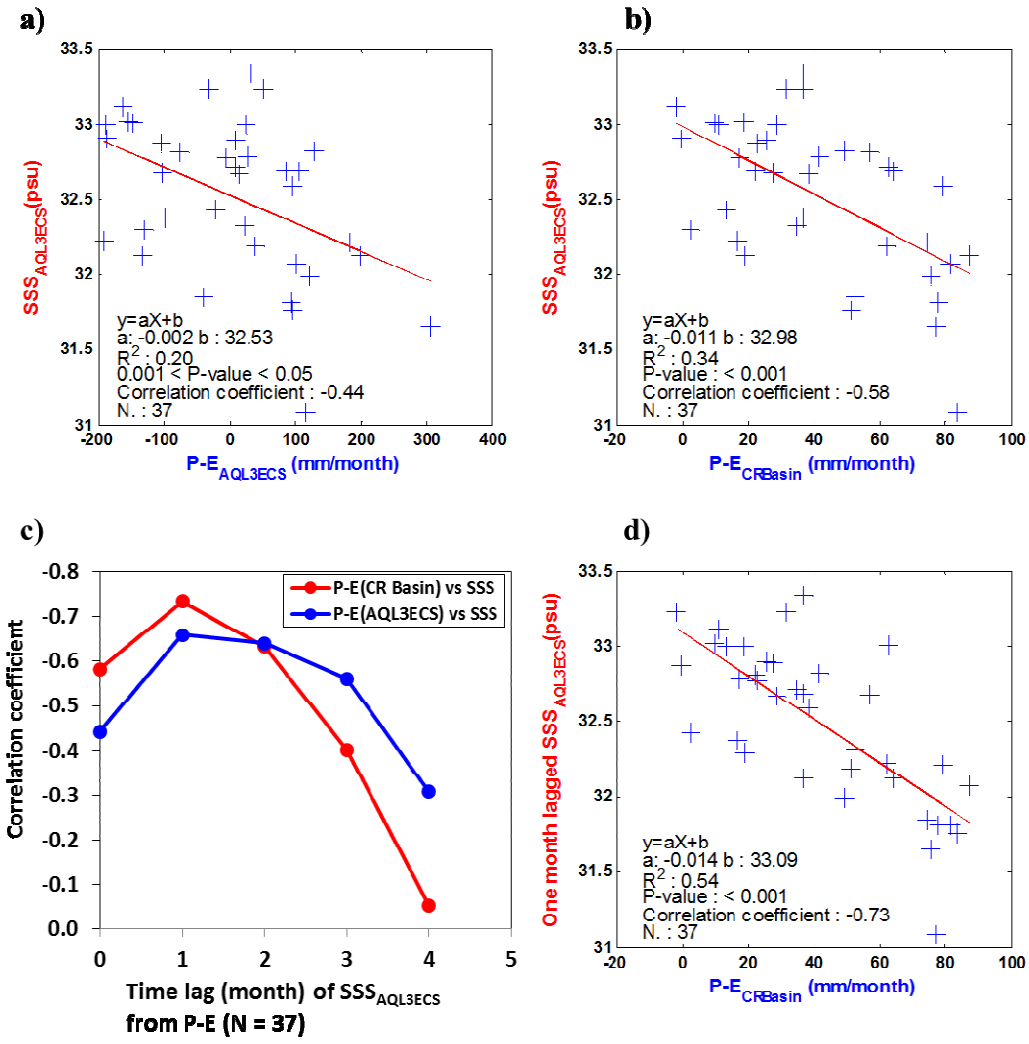

Figure 17. Scatter plot of monthly a) $SSS_{AQL3ECS}$ and $P\text{-}E_{CR\ basin}$, b) $SSS_{AQL3ECS}$ and $P\text{-}E_{AQL3ECS}$, c) Correlation coefficient by monthly time-lagged SSS with P-E(CR Basin : red, AQL3ECS : blue), d) Scatter plot of monthly $P\text{-}E_{CR\ basin}$ and one-month lagged $SSS_{AQL3ECS}$

Time lagged relationships between $SSS_{AQL3ECS}$ and $P\text{-}E_{CRBasin}$ (red solid line), $SSS_{AQL3ECS}$ and $P\text{-}E_{AQL3ECS}$ (blue solid line) were investigated (Figure 17c). Accordingly, a strong negative correlation between $SSS_{AQL3ECS}$ and $P\text{-}E_{CRBasin}$ was found for a one to two month-time lag (-0.73 at one month and -0.63 at two-month lag). A one month-time lag correlation was also found between $SSS_{AQL3ECS}$ and $P\text{-}E_{AQL3ECS}$ with a lower correlation coefficient (-0.66 at one month and -0.64 at two month lag, blue solid line) than $SSS_{AQL3ECS}$ and $P\text{-}E_{CRBasin.}$ A similarly lagged relationship between SSS and P-E was found in the river outflowing coastal Atlantic Ocean (Chao et al., 2015; Da-Allada et al., 2014; Tzortzi et al., 2013).

The one month time-lagged negative correlation (-0.73) between $SSS_{AQL3ECS}$ and $P\text{-}E_{CRBasin}$ is a better correlation than reported in Kim et al. (2014) for the lagged correlation (30–50 days) between Aquarius SSS and river discharge (-0.71). These results are consistent with earlier studies and indicate a phase lag between precipitation over mainland China and river discharge (Delcroix & Murtugudde, 2002; Ferreira et al., 2013). Therefore, the temporal variation of SSS in the ECS is affected by river runoff from the mainland China at a one-month-time lag from integrated P-E.

Summary

By selecting Aquarius L3 SSS data which is at least 150 km from the coast (the region denoted AQL3ECS), Aquarius L3 SSS of ASC passes showed better agreement with in situ SSS than that of DSC passes (negative bias about -0.34 psu smaller than descending pass bias of -1.37 psu). However, the bias in the DSC passes did show a decreasing trend that is probably due to the elimination of RFI sources in the region.

The monthly averaged $SSS_{AQL3ECS}$ shows not only a statistically significant relationship with P-E, but also strong negative correlation at a one-month lag (-0.73

with $P\text{-}E_{CRBasin}$, -0.66 with $P\text{-}E_{AQL3ECS}$). This implies that L3 SSS, which is flagged as likely suffering from severe contamination, can be used by only utilizing data from the ASC passes and then only data taken at least 150 km from the coast. If RFI sources are better mitigated in the future, utilization of L3 SSS from descending passes may be possible.

APPENDIX B

Position coordinates for making AQL3ECS (see red polygon in the Figure 12a)

	Longitude	Latitude		Longitude	Latitude
1	122.0	35.0	12	123.0	27.0
2	122.0	33.0	13	126.0	27.0
3	123.0	33.0	14	126.0	28.0
4	123.0	32.0	15	128.0	28.0
5	124.0	32.0	16	128.0	32.0
6	124.0	31.0	17	125.0	32.0
7	125.0	31.0	18	125.0	33.0
8	125.0	30.0	19	124.0	33.0
9	124.0	30.0	20	124.0	35.0
10	124.0	28.0	21	122.0	35.0
11	123.0	28.0			

Estimation of freshwater flux (P-E)

1. P-E in the CR Basin (see blue polygon at Figure 12b)

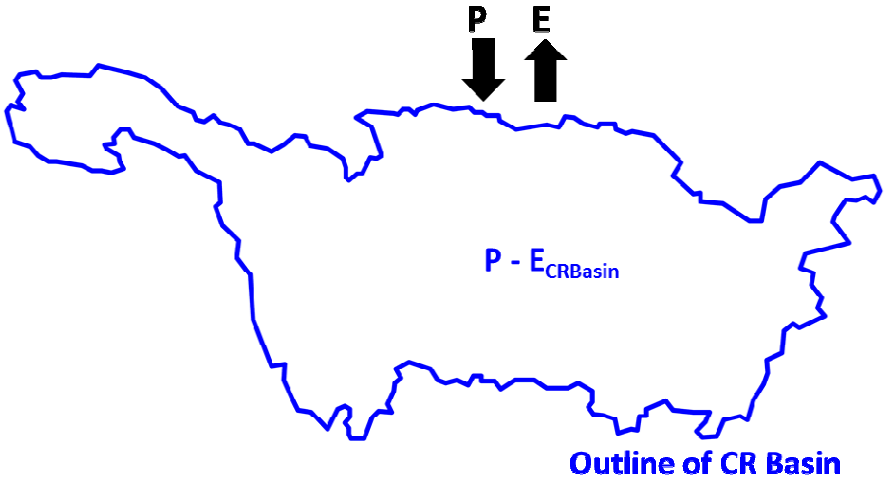

P: Monthly precipitation from TRMM (3B43) (mm/month)

E: Monthly evaporation from (GLDAS) (mm/month)

$P\text{-}E_{CRBasin}$: Monthly freshwater flux

2. P-E in the AQL3ECS

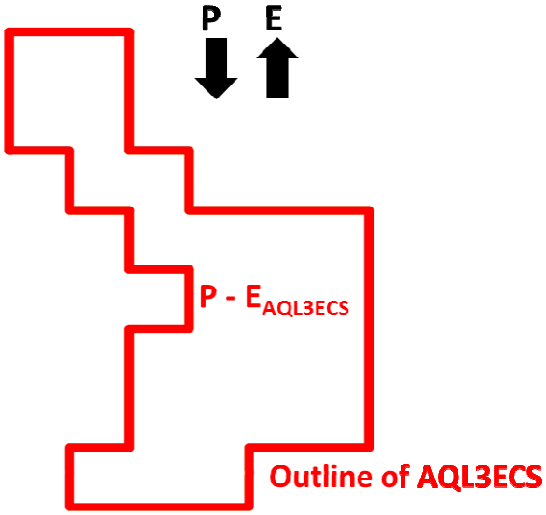

P: Monthly precipitation from TRMM (3B43) (mm/month)

E: Monthly evaporation from (OAFlux) (mm/month)

$P - E_{AQL3ECS}$: Monthly freshwater flux averaged in AQL3ECS area

Estimation of P-value between SSS and P-E (Hypothesis test)

1. Estimate the correlation coefficient (Pearson's correlation coefficient) between SSS and P-E:

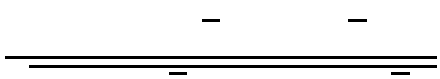

Where, : Monthly P-E of CR basin (or the ECS), Monthly $SSS_{AQL3ECS}$

: Correlation coefficient between SSS and P-E

2. Estimate test statistic of T-test

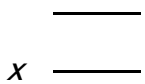

Where, - 2: Degree of freedom,

r : Correlation coefficient between SSS and P-E

3. Estimate *P- value* using Excel function (TDIST)

P- value = TDIST(ABS(t), n-2, 2)

Where, TDIST: Two-tailed probability in the Student t-distribution table for the given test statistic value and number of degrees of freedom

n - 2: Degrees of freedom, : Correlation coefficient between SSS and P-E

t : Test statistic value

4. Hypothesis test for SSS and P-E using *P-value* for the present dissertation:

If *P- value* $\geq$ 0.05: SSS and P-E have no statistical significance

0.001 < *P- value* < 0.05: SSS and P-E have statistical significance

P- value < 0.001: SSS and P-E have strong statistical significance

CHAPTER III

ANALYSIS OF SMOS SSS

Method and Materials

Investigation of RFI flags in ECS

In the ECS, the monsoon season of June-September, 2014 was selected for the SMOS L2 OS product of version 550 (Downloadable using ESA's Earth Observation Link (EOLI); http://earth.esa.int/EOLi/EOLi.html; filename begins with "SM_OPER _MIR_OSUDP2"). The amount of available measurements after SMOS RFI flagging was calculated as a percentage of available measurements (100×Number of passes which is non-RFI flagged/Total passes) for combined passes for 25 × 25 km resolution of independent pixels (e.g., If 3 passes out of total 10 passes were not RFI flagged for a single pixel during certain length of time, the percentage of available measurements for the pixel is 30%; see Appendix C). As shown in figure 18a, around half of the total passes were shown available after using the outlier detection flag (Fg_ctrl_many_outlier, SMOS TEAM, 2008), and utilizing only L2 SSS ± 300 km from the center of the swath (Boutin et al., 2012; Chuprin & Font, 2012) in the ECS. However, the acceptable passes were greatly decreased if the suspicious RFI flag (Fg_ctrl_suspect_rfi; Figure 18b) was used, and there we no acceptable passes in the ECS if the acceptable quality flag (Fg_Ctrl_Chi2_P; Figure 18c) was used. Even though the average RFI probability considerably decreased in 2014 (Figure 10e), many measurements are still flagged as RFI contaminated because most of the grid points show the RFI probability higher than the threshold of Fg_ctrl_suspect_rfi (> 33 %). Moreover, the majority of L2 grid points are flagged as having their Chi2P (Chi square probability: acceptable probability) for the T_b and other auxiliary parameters (e.g., WS, SST) as less than 0.05 in the RFI dominated region (the

threshold of Fg_Ctrl_Chi2_P is $0.05 \leq \text{Chi2P} \leq 0.95$ from the Chi-square distribution, see Table 4 in Appendix A). Thus, existing SMOS RFI flags need to be carefully modified to collect SSS in the ECS.

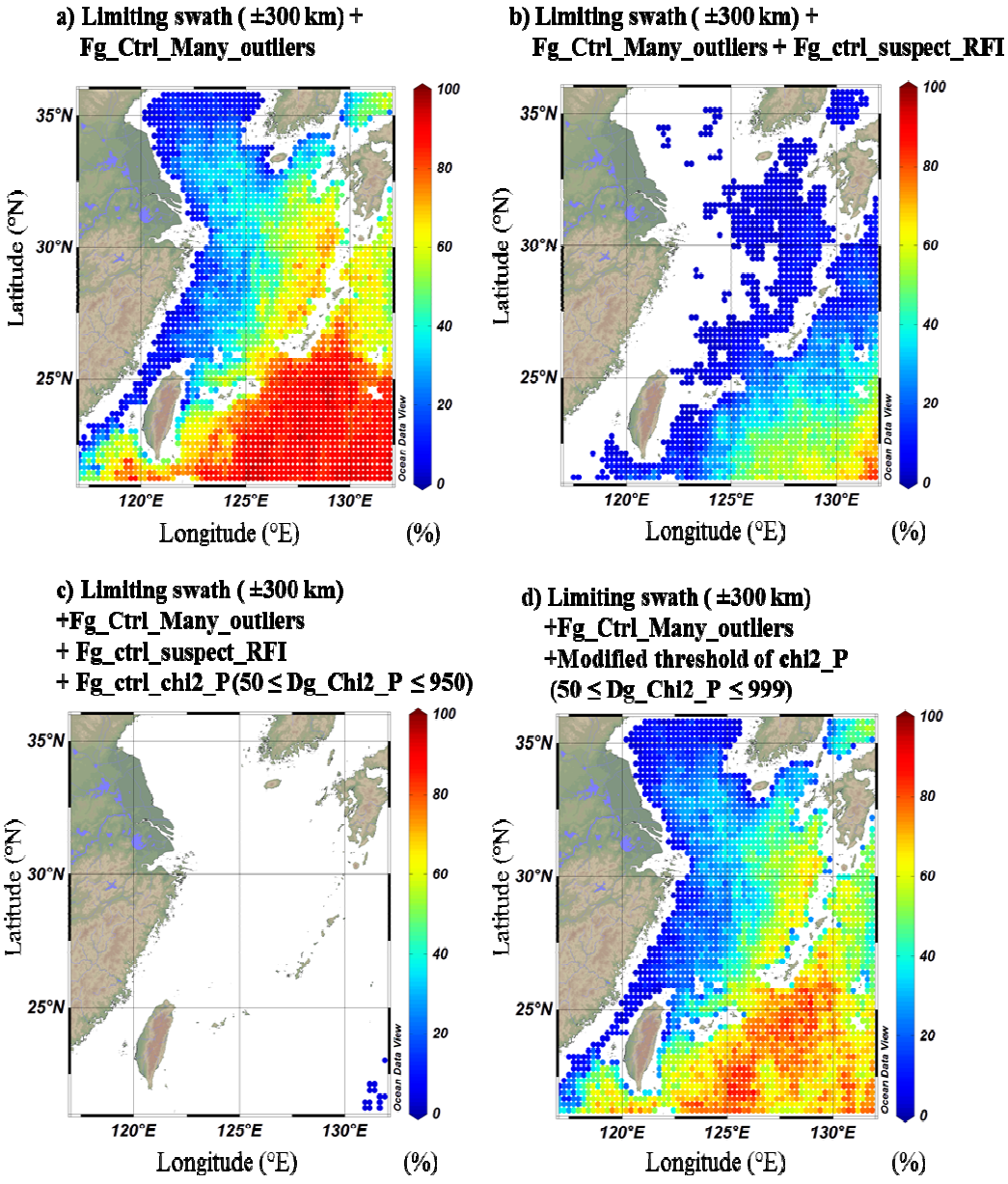

Figure 18. Map of percentage for available L2 measurement of SMOS for the single grid point (a–c : applying existing RFI flags, d : empirical modification of RFI flags) in June–September, 2014.

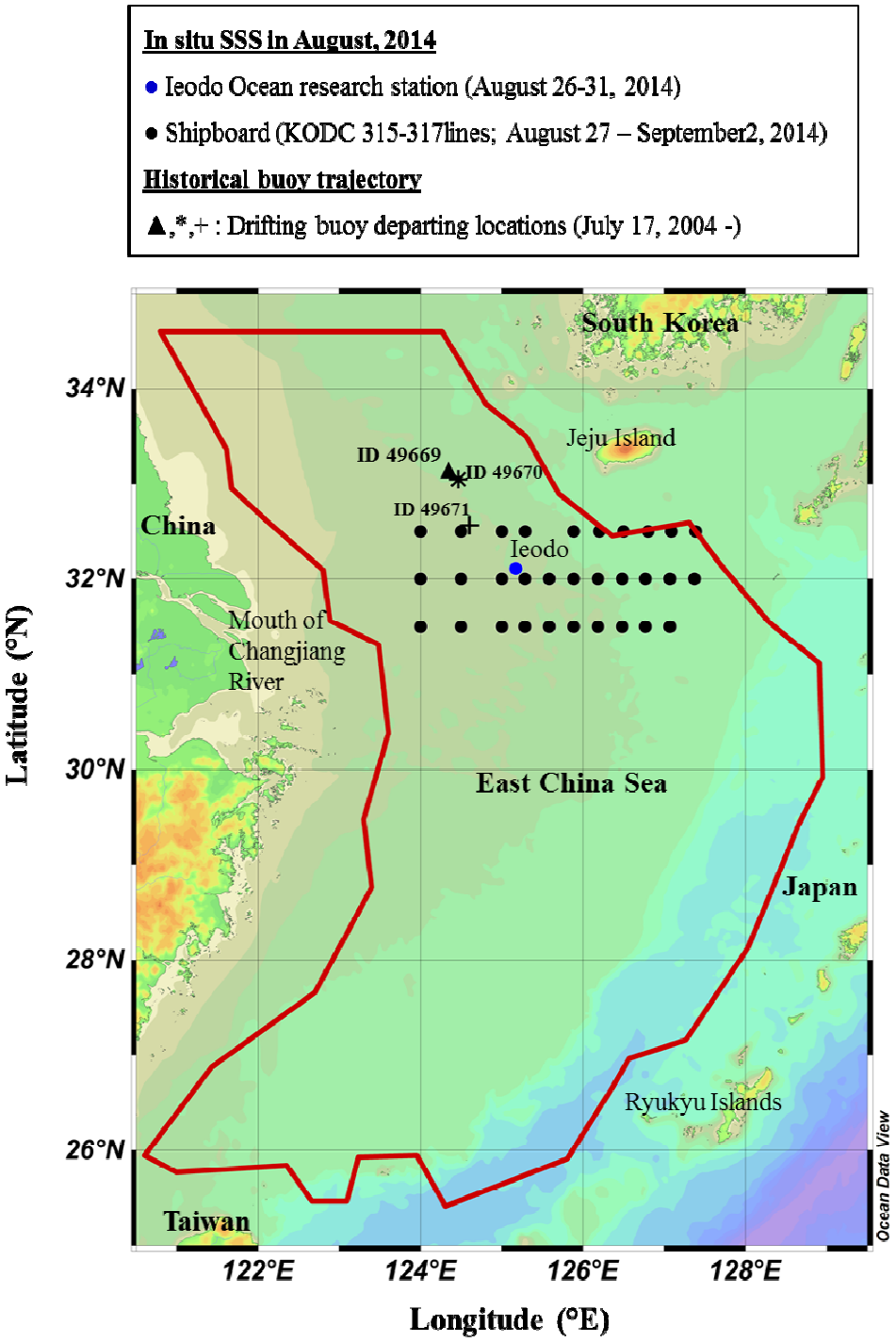

Figure 19. Experimental area for SMOS SSS (Red polygon is the area of $SSS_{SMOS\ ECS}$). In situ observations are shown in the legend above the figure.

Regional organization of SMOS flags (SMOSECS)

In order to find more usable SMOS SSS measurement in the ECS, a new procedure for utilizing SMOS RFI flags was developed, which focuses on removal of severe contamination by RFI. First, the flag Fg_ctrl_many_outliers was used and only SSS ±300 km from the center of the swath was used to reduce suspicious grid points with large deviated T_b from all incidence angle (Chuprin & Font, 2012; Zine et al., 2008). This procedure deviated from the normal practice of using the flag Fg_ctrl_suspect_RFI, which would result in throwing out too much data. Next, we empirically modified the low limit threshold of Chi2P from 0.05 to 0.001 to collect enough amount of sample by increasing Dg_chi2P from 950 to 999 (SMOS L2OS processor indicates Chi2P by Dg_chi2P as Dg_chi2P/1000 = 1-Chi2P, see Table 1 in Appendix C; Chuprin & Font, 2012). By this modification, the present dissertation does not allow a zero value of Chi2P (i.e., 1000 of Dg_chi2P), which indicates 100 % contamination. In addition, the potential risk for RFI and land contamination near the coast were minimized by limiting the collecting area to be >100 km from the coast (Gabarró et al., 2012; Zine et al., 2007), by using the "land-sea mask" flag in the L2 product (SMOS TEAM, 2008; red solid line in Figure 19). The utilization of the SMOS flags for the ECS, developed for this dissertation, is referred to as "SMOSECS" (See Table 1, 2 in Appendix C).

There are also several geophysical parameters of which limiting thresholds are required to prevent biases in SSS (e.g., Wind speed (WS), and sea surface temperature (SST); Chuprin & Font, 2012). The present dissertation uses a regionally set of thresholds. For SST and WS, the choices of Ren et al. (2015) for the SCS were used: $10 \leq SST \leq 30°C$ and $3 \leq WS \leq 10$ m/sec. Here, the threshold of WS is applicable for comparing three types of SMOS roughness correcting algorithms for

the L2 product (See Table 2 in Appendix A). The other flags (e.g., cosmic galactic, sun/moon glint noise, heavy rain (>10 mm/hr) and ice impact to the T_b) were applied based on global threshold by Chuprin & Font (2012). Because spatial and temporal average of the swaths was reported to decrease the uncertainty of the SMOS SSS (Mecklenburg et al., 2012; Boutin et al., 2012; Font et al., 2013), averaging was conducted over 10 days and 25×25 km after using the new procedures for utilizing the data quality control flags for SMOS L2 SSS (here the final product is named as $SSS_{SMOSECS}$).

Table 5

Dataset for experiment for SMOS L2 SSS

Data	Mission	Purpose
1. SSS (Remote sensing)	SMOS (L2)	Produce SSS from re-organized flags "SMOSECS"
	Aquarius (7days; AQL3ECS)	Comparing with $SSS_{SMOSECS}$
2. Wind velocity (Remote sensing)	Windsat (Daily)	Infer the spatial variability of SMOS retrieved SSS
3. Rain rate (Remote sensing)	TRMM (Daily)	Precipitation
4. SSS (Insitu)	KODC Ieodo ocean research station (Temporally Averaged SSS)	Examine the accuracy of $SSS_{SMOSECS}$
5. Historical Trajectory (drifters)	AOML	Infer the spatial variability of $SSS_{SMOSECS}$

The selection of SMOS SSS data based upon the new use of the flags was conducted via the SMOS product reader added in the Brockmann Consult's BEAM VISAT 5.0 software (Downloadable at http://www.brockmann-consult.de/cms/web/beam/). Using VISAT software, spatial averaging was performed over 25×25km areas to reduce noise, but still capture the small-scale spatial variability (relative to Aquarius). The best agreement algorithm (as one of Alg.1-3) was selected by comparing SMOS SSS (25 × 25 km) with in situ SSS.

Comparison between SMOS and in situ SSS

Although it is common to compare SMOS SSS with Argo float SSS (Boutin et al., 2012; Reul et al., 2012), the shallow continental shelf of the ECS (< 100 meters) results in fewer available floats (the floats normally go down to thousand meter depth), and freshwater sources can cause differences between SSS and the salinity at the shallowest depth (about 5 meter below surface) sampled by Argo floats (Boutin et al., 2013; Tang et al., 2014). Upon examining the few available coincident Argo float data (August 6–14, 2014) near the Ryukyu Islands, we found that SSS of these floats were biased high, potentially due to rainfall associated with Typhoon Halong, moving toward Japan. For these reasons, $SSS_{SMOSECS}$ was, instead, compared with NFRDI shipboard in situ SSS in August, 2014 (see black dots in Figure 19).

Because shipboard CTD measurement was measured with limited amounts in August in 2014, we had to search for additionally available in situ SSS. Data from the Ieodo ocean research station (see blue dot in Figure 19), operated by Korea Hydrographic and Oceanographic Administration (KHOA), was found to be in the region of interest (available at Korea Ocean Observing and Forecasting System (KOOFS), http://sms.khoa.go.kr/koofs; Table 6). The station observes SSS hourly (blue dot in Figure 19). Since the SSS from this station was not always available in

August, because biofouling contaminates the salinity sensor (Shim et al., 2009), the time series of SSS was averaged for the dates of NFRDI shipboard measurement at the same month (Table 6). The collocation between SMOS and in situ SSS was conducted within 0.1 degree radius from the in situ stations. Finally, the accuracy of whole collocated samples was tested by estimating Root Mean Square Error (RMSE) (Appendix C). A geometric mean (GM) regression method (Ricker, 1973) was also used to determine the slope between collocated SMOS and in situ SSS (Appendix C).

Table 6

Outline of comparison between SSS_{SMSECS} and SSS_{Insitu}

Dates of SMOS L2 for composite (MM/DD)	Dates of in situ SSS (MM/DD)	Number of collocated samples
1. ASC (4) and DSC (4) : 8/26, 8/29, 8/31, 9/3	Ship board (NFRDI) SSS : 8/27–9/2	18
	Stationary SSS (Ieodo Ocean research station) : 8/26–8/31	1
2. Total number of samples for comparison		19

Investigation of spatial variability of SMOS

For the dates for which the percentage of SMOS L2 data that passed quality control checks was relatively high, the capability of SMOS to demonstrate spatial variability was investigated in 2014. Three Historical drifting buoys (ID 49669, 49670, 49671) collected by the Atlantic Oceanographic and Meteorological

Laboratory (AOML; data available at the Global Drifter Program web page, http://www.aoml.noaa.gov/phod/dac/index.php) were used to compare the location of low salinity water and the buoy trajectories (see the departing locations in figure 9). Additionally, daily wind velocity from WindSat, that is the payload on the Air Force Coriolis satellite, was employed to discover the relationship between southeasterly wind and spatial variation of SSS (WindSat data is downloadable at http://www.remss.com/missions/windsat; Table 5). The $SSS_{SMOSECS}$ (10 days averaged, 120×120 km averaged) and 7 days averaged L3 $SSS_{AQL3ECS}$ were compared with each other to determine the differences between the data sets. Using the NASA Giovanni tool (http://disc.sci.gsfc.nasa.gov/giovanni), the daily precipitation from TRMM (3B42) in the CR estuary was used to investigate the low salinity spatial feature near the mouth of the CR (Table 5).

Result and discussion

Available measurements using SMOSECS flags

As shown in Figure 20, the percentage of available L2 measurements filtered by SMOSECS flags for monthly averaged SSS (here Alg.3 was nominally selected) are shown for independent satellite passes for June–September in 2014. Ascending passes have greater amounts of available measurements than descending passes for the whole ECS (compare ascending passes in Figure 20 and descending passes in Figure 21).

The relatively small amount of measurements in the descending passes are likely due to high RFI probability (Table 7), which might be caused by land RFI sources that are different up to the overflight pass (Figure 9). Both for ascending and descending passes, the spatial amount of the available distribution shows a dependence on RFI probability (i.e., larger number of available measurement as lower

RFI probability, the smaller amount of gridpoints as higher RFI probability). For this reason, SMOSECS flags appropriately work to reduce RFI contamination without utilizing the suspicious RFI flag, which throws out most of the data.

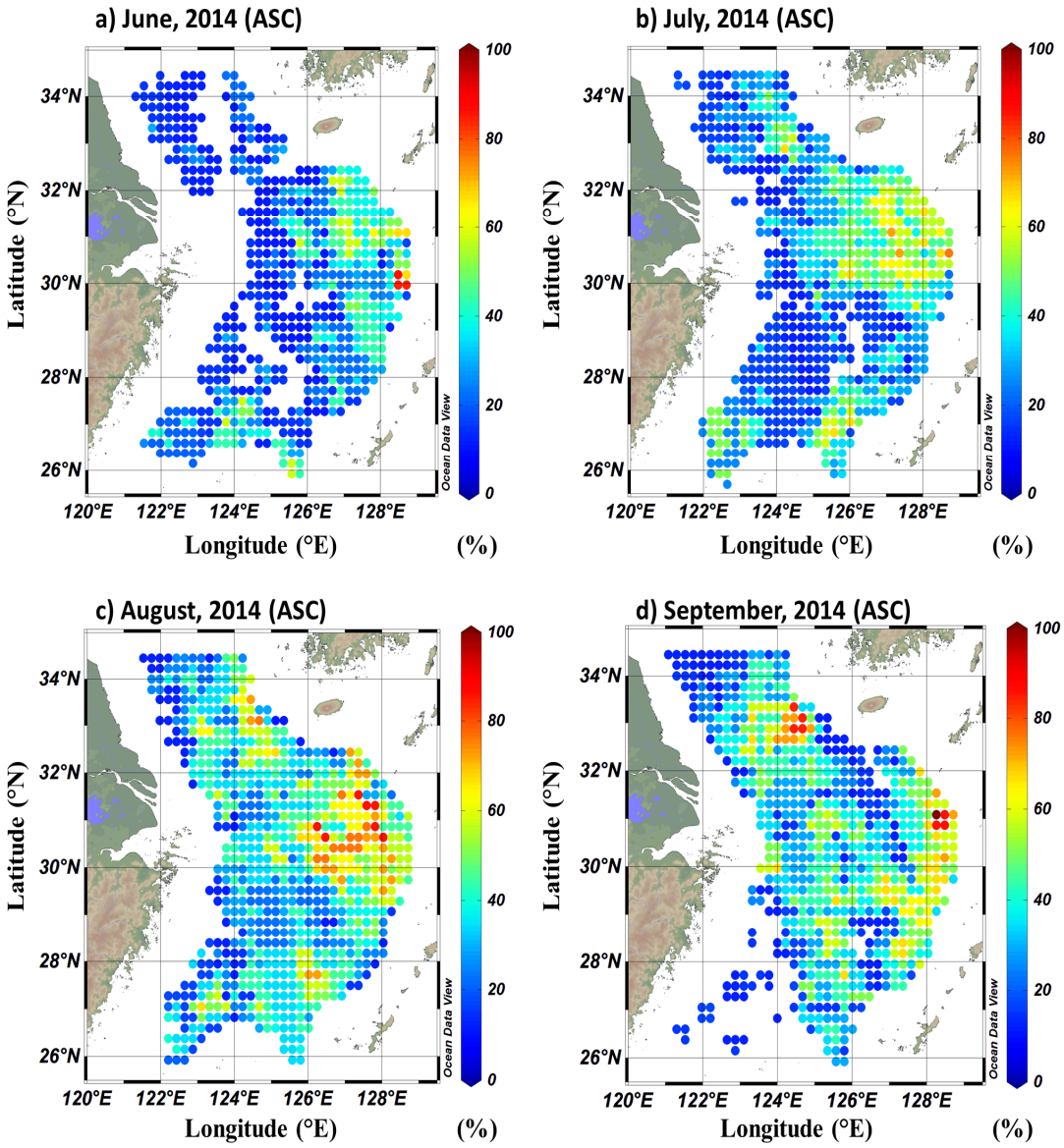

Figure 20. Map of percentage of available L2 measurement of SMOS for the single grid point after applying SMOSECS flags in the ECS from June to September, 2014 (Ascending pass; No data in the white area).

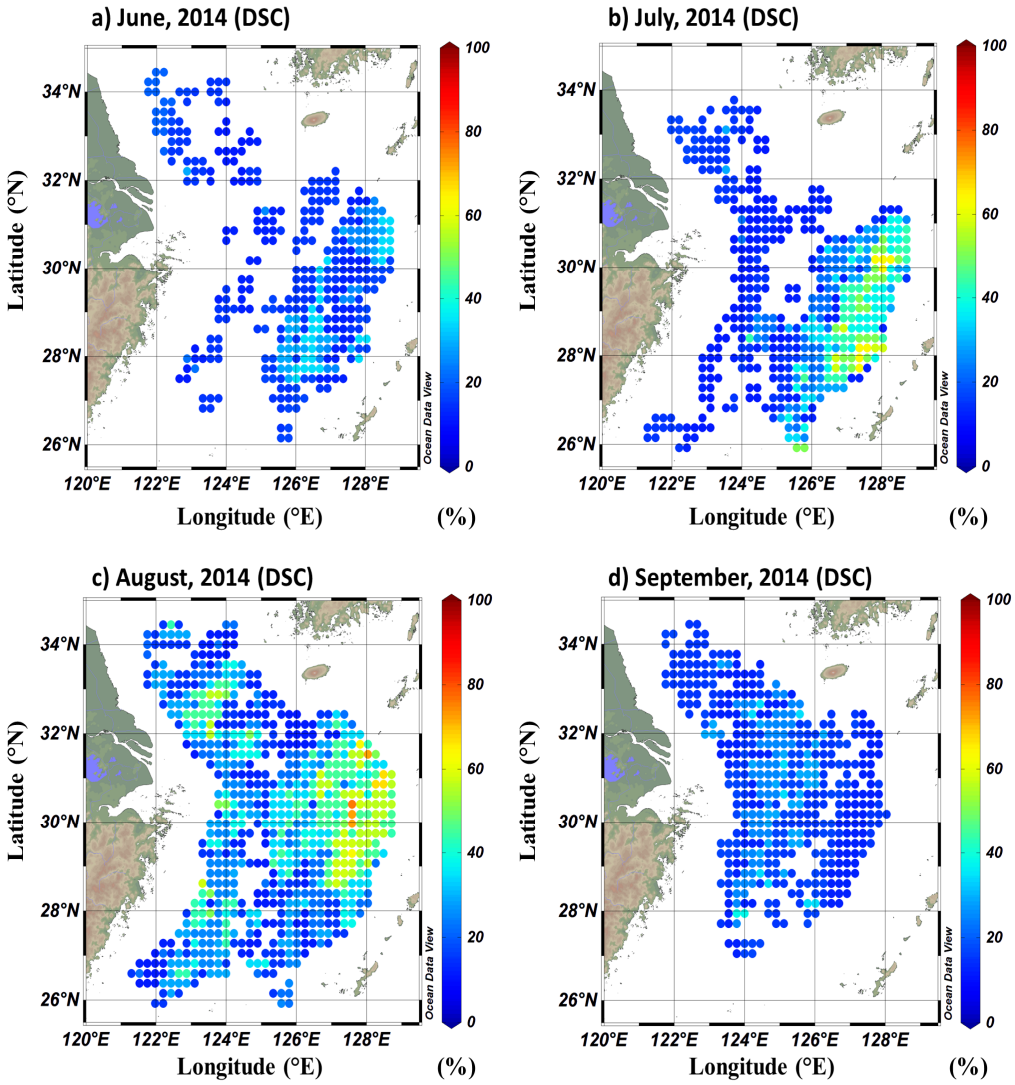

Figure 21. Map of percentage for available L2 measurement of SMOS for the single grid point after applying SMOSECS flags in the ECS from June to September, 2014 (Descending pass; No data in the white area).

Comparison between SMOS and in situ SSS

In order to examine $SSS_{SMOSECS}$ with enough number of collocated in situ samples over the ECS, we compared spatial (25×25km) and 9days temporally averaged (August 26–Septempber3, 2014) $SSS_{SMOSECS}$ with in situ SSS from NFRDI and Ieodo ocean research station (Table 6). Three algorithms of $SSS_{SMOSECS}$ resulted in a

positive bias (0.144–0.337 psu) in ascending (Figure 22a–c), and negative bias (-0.221– -0.150 psu) in descending (Figure 22d–f) passes relative to situ SSS.

Table 7

Mean percentage of available measurements of SMOS with RFI probability in the ECS

	Swath	June, 2014	July, 2014	August, 2014	September, 2014
1. Percentage of available measurements from L2 swath (%)	ASC	24.49	30.34	37.83	35.03
	DSC	17.78	22.55	28.64	17.21
2. RFI probability in the ECS (%)	ASC	57.1	53.36	52.3	54.83
	DSC	59.53	56.7	53.25	56.26

This bias was successfully reduced (-0.039–0.085 psu) by combining ascending and descending passes (Figure 22g–i) showing smaller biases than those found in previous studies in the SCS and Northwestern Pacific Ocean (NPO) (Table 8). In addition, the range of the bias shown in the combined passes is close to the bias of globally used Level 3 SSS (-0.23–0.04 psu) from Centre Aval de Traitement des Données SMOS (CATDS, http://www.catds.fr) (Reul et al., 2014a, Table 2).

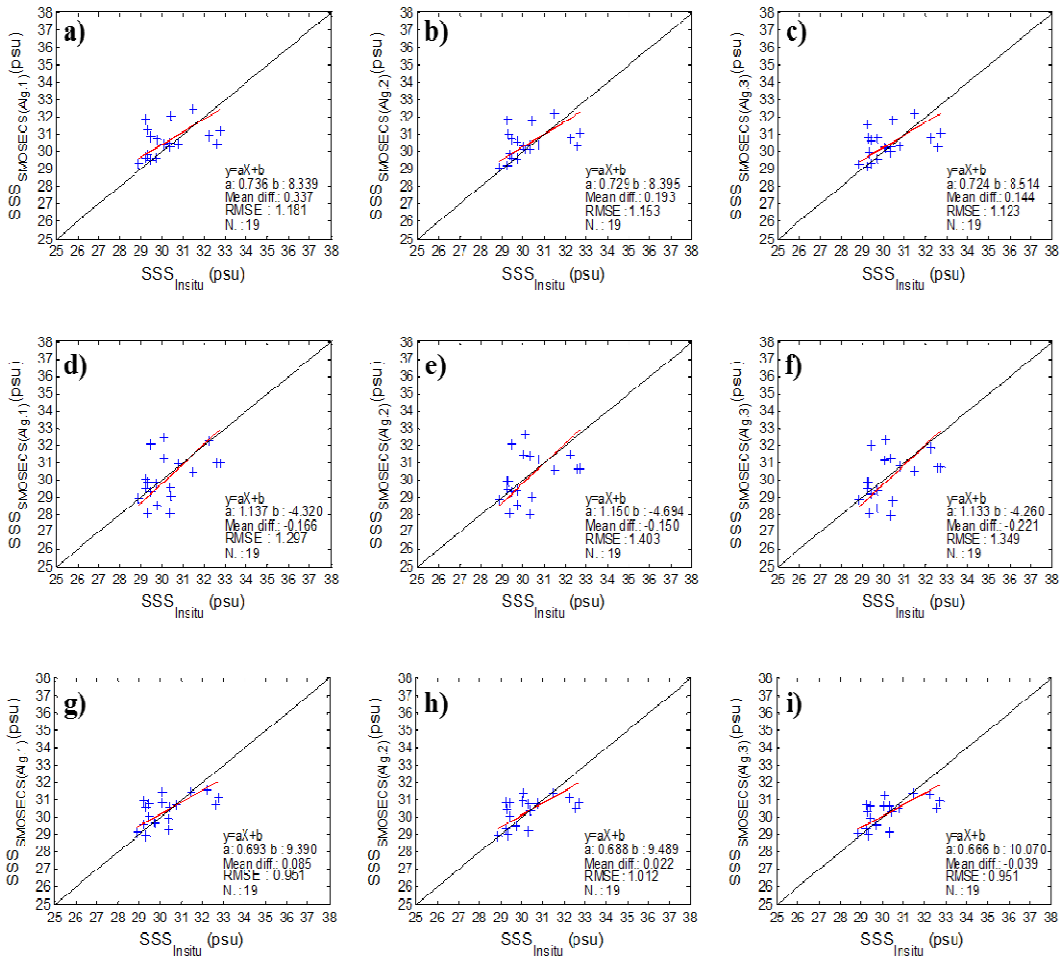

Figure 22. Comparison between $SSS_{SMOSECS}$ (9 days; 25×25 km) and SSS_{insitu} for ascending (a–c), descending (d–f), ascending+descending passes (g-i)

In terms of accuracy, as shown in the comparison in the figure 22, for the independent passes, RMSE ranges 1.123–1.403 psu which appears higher than the RMSE of globally mapped SSS (~0.5 psu) from CATDS (Reul et al., 2014b). Although this RMSE is non-negligible, it still results in usable information in the ECS where previous studies have not been able to find any. In addition, the reduced RMSE (0.951–1.012 psu) that results by combining ascending and descending passes shows the improvement of using spatial and temporal averaging of swaths as demonstrated in the SCS by Ren et al. (2015; Table 8). Moreover, inconsistently low or high SSS

Table 8

Comparison of the bias of $SSS_{SMOSECS}$ with the case in South China Sea

	Algorithm	East china Sea (This research)		South China Sea (0.05° × 0.05°; Ren et al., 2015)		Northwestern pacific Ocean (Wang et al., 2014)
		Diff.	RMSE	Diff.	RMSE	
1. Ascending Pass	Alg.1	0.337	1.181	-0.141	0.979	
	Alg.2	0.193	1.153	-0.100	0.928	Diff. : -0.35 psu
	Alg.3	0.144	1.123	-0.137	0.941	
2. Descending Pass	Alg.1	-0.166	1.297	-0.720	1.28	
	Alg.2	-0.150	1.403	-0.756	1.279	
	Alg.3	-0.221	1.349	-0.706	1.248	
3. Ascending + Descending Pass	Alg.1	0.085	0.951	-0.469	0.851	
	Alg.2	0.022	1.012	-0.464	0.814	
	Alg.3	-0.039	0.951	-0.428	0.795	

did not occur in the averaged data set, and the geometric mean slope between SMOS and in situ SSS shows positively close to unity (0.666–1.150; Figure 22). Here, Alg.3 of SSS with combined ascending and descending passes is selected as the best

$SSS_{SMOSECS}$ for the ECS because of low RMSE (0.951 psu) and bias (-0.039 psu) of the three algorithms.

Investigation of spatial variability of SMOS SSS

SSS (Alg.3) combined by ascending and descending passes (here we use $SSS_{SMOSECS}$) and $SSS_{AQL3ECS}$ was compared during July–September, 2014 separated by period 1–period 6 (SMOS 10 days, Aquarius 7 days averaged SSS, table 9). For Aquarius, seven days averaged SSS of L3 ascending pass ($SSS_{AQL3ECS}$) was selected as close to the dates of beginning dates with SMOS SSS (Table 9).

In period 2, both Aquarius and SMOS coincidently show low salinity (< 28 psu) near the CR mouth (Figure 23 b, e). This low SSS was described as "extremely low salinity" comparing the usual ranges of low salinity of 28–32 psu near the Jeju Island (Hyun & Pang, 1998; Moon et al,. 2012). This extremely low salinity was used as an indicator of CDW extending into the region near Jeju Island, forced by alongshore wind (southeasterly wind) inducing surface Ekman flow after typhoon passage through mainland China (Moon et al,. 2012). This occurred in 1996 (Moon et al,. 2010).

Interestingly, when Typhoon Matmo passed through Taiwan on its way to mainland China, changing its status to tropical storm (July 21–25, 2014; Figure 25), the expansion of extremely low salinity was coincidently captured (see white dashed line in Figure 23 b, e) from both Aquarius and SMOS in period 2.When the storm arrived in China on July 23–24, 2014 (Figure 25), southeasterly winds of 6.72–10.74 m/sec prevailed near the mouth of the CR (122°–126° E, 29°–34° N; Figure 26a, d),

Table 9

Comparison between $SSS_{SMOSECS}$ and $SSS_{AQL3ECS}$

	Dates of L2 swaths of $SSS_{SMOSECS}$ combined into 10-day composites (MM/DD)	Dates of weekly averaged SSS of Aquarius/SAC-D V.3 (MM/DD)
1. Period 1	ASC(5): 7/11, 7/13, 7/16, 7/21 DSC(5): 7/11, 7/16, 7/21	ASC : 7/16 – 7/22
2. Period 2	ASC(5),DSC(5) : 7/21, 7/24, 7/26, 7/29, 7/31	ASC : 7/23 – 7/29
3. Period 3	ASC(5): 7/31, 8/3, 8/5, 8/8, 8/10 DSC (5) : 7/31, 8/1, 8/3, 8/6, 8/8	ASC : 7/30 – 8/5
4. Period 4	ASC (6): 8/10, 8/13, 8/15, 8/16, 8/18, 8/21 DSC (5): 8/11, 8/13, 8/16, 8/18, 8/21	ASC : 8/13 – 8/19
5. Period 5	ASC (6): 8/21, 8/23, 8/26, 8/28, 8/29, 8/31 DSC (5): 8/21, 8/24, 8/26, 8/29, 8/31	ASC : 8/20 – 8/26
6. Period 6	ASC (5): 8/31, 9/3, 9/5, 9/8, 9/10 DSC (4): 8/31, 9/3, 9/5,9/8	ASC : 8/31 – 9/10

and TRMM daily averaged precipitation in the estuary (117°–122° E, 29°–34° N) rapidly increased up to 29.8 mm/day, with 194.7 mm/day maximum precipitation rate (Figure 26 b, c). Thus, it is likely that Aquarius and SMOS captured extremely low salinity affected by wind-driven Ekman flow in period 2.

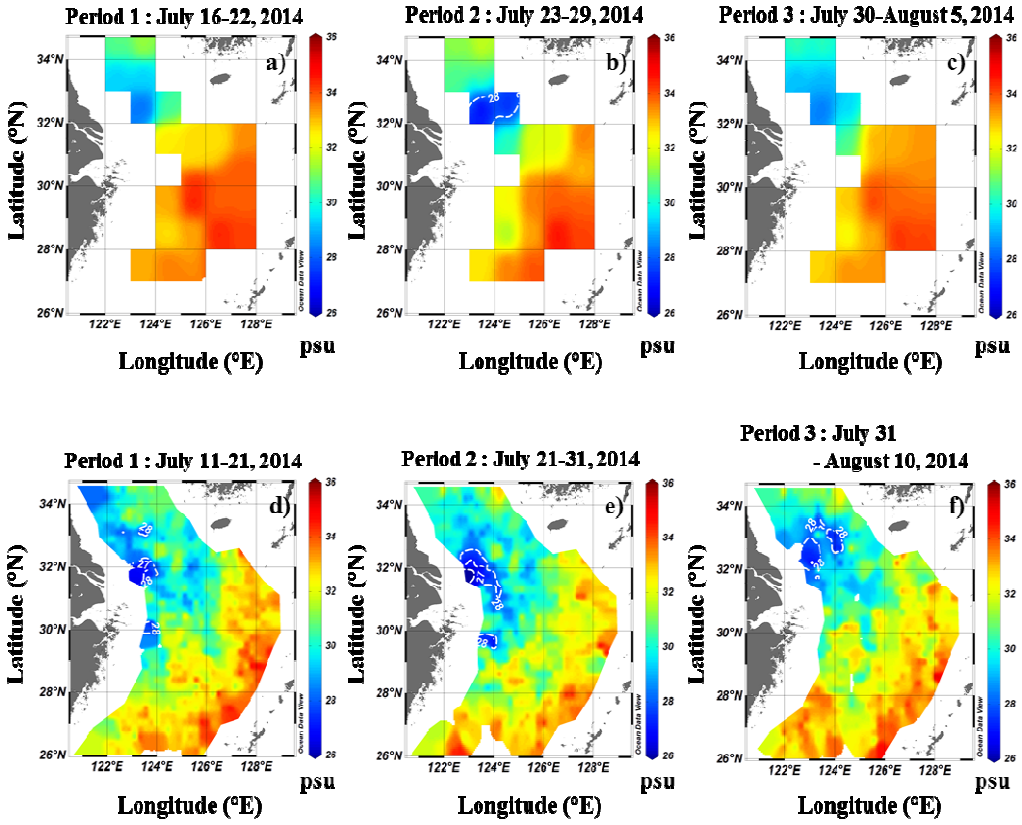

Figure 23. Horizontal map of 7 days $SSS_{AQL3ECS}$ (a-c) and $SSS_{SMOSECS}$ (10 days; 25×25 km; d–f) during period 1–3 (White colored dashed line represents low salinity less than 28 psu).

While this extremely low salinity water was captured only once from Aquarius (Figure 23b), SMOS captured the SSS several times (Figure 23d–f, Figure 24e). For instance, the isolated patch of extremely low salinity water away from the main body of the CDW in period 3 (Figure 23f) likely represents the detachment of CDW.

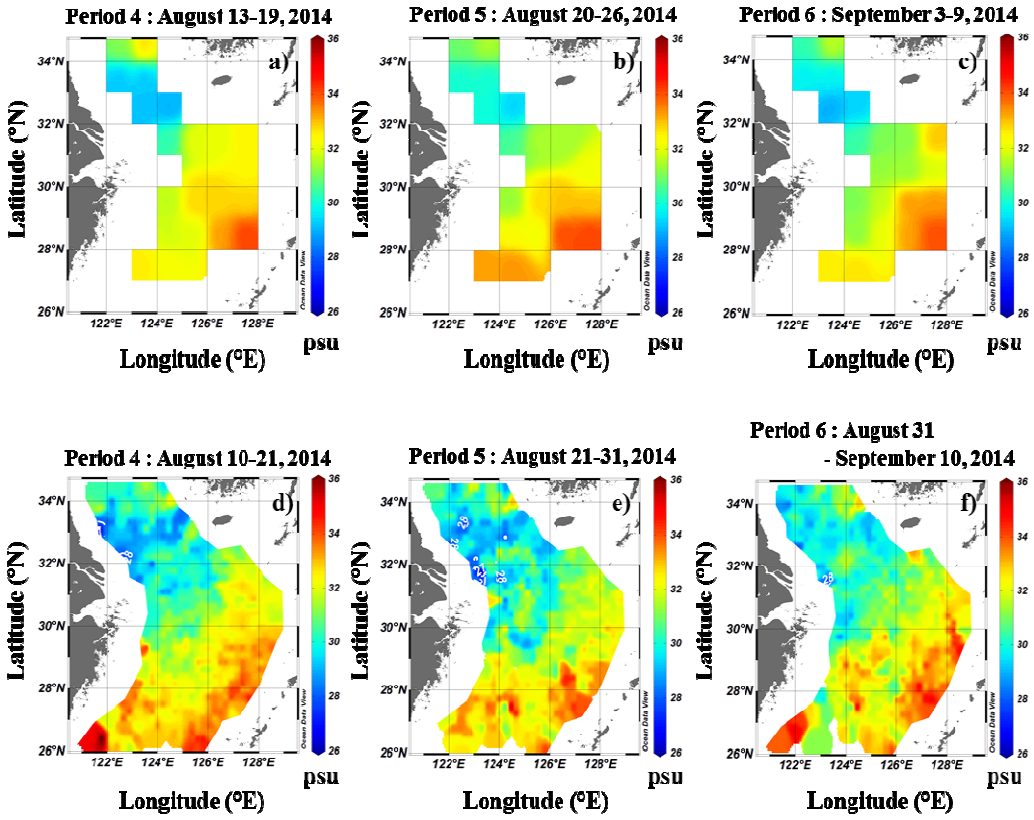

Figure 24. Horizontal map of 7 days $SSS_{AQL3ECS}$ (a–c) and $SSS_{SMOSECS}$ (10 days; 25×25 km; d–f) during period 4–6 (White colored dashed line represents low salinity less than 28 psu).

According to the suggestion of Xuan et al. (2012) that a northeastward detachment of CDW is enhanced when the alongshore (Southeasterly) wind increases to higher than 8 m/sec, this isolated low salinity patch might have resulted from the increased southeasterly wind speed (6.72–10.74 m/sec) in period 2 (Figure 26a).

On the other hand, the low salinity patch was not captured in Aquarius for period 3 implying that Aquarius mostly observes large-scale movement of CDW from mainland China (Figure 23c) because the size of the patch is about 80 km diameter, which is smaller than the spatial resolution of Aquarius (150 km×150 km), but detectable by the high resolution of SMOS (25×25 km).

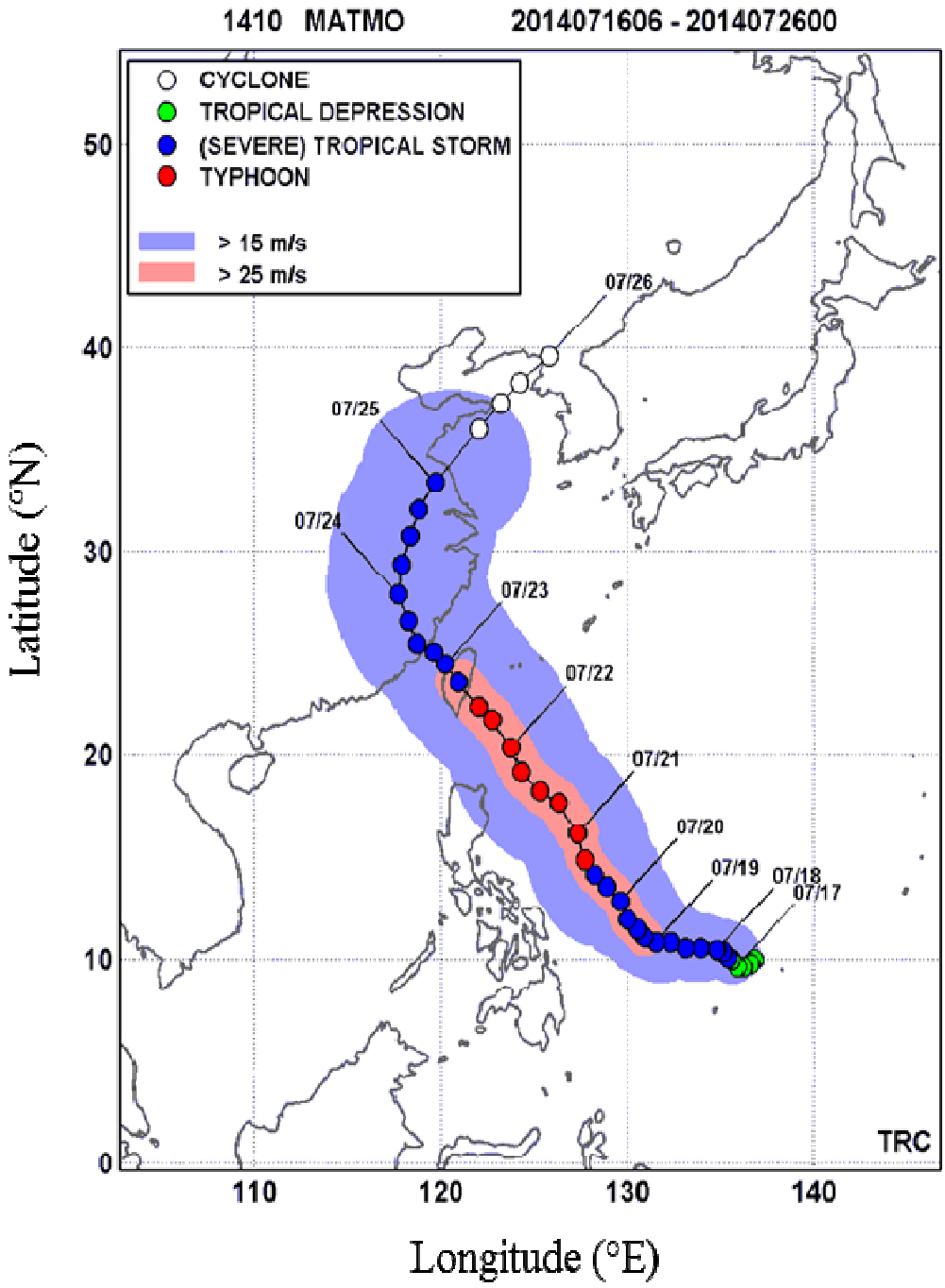

Figure 25. A path of the Typhoon Matmo (July 16–26, 2014; Image credit: Typhoon research center at http://www.typhoon. or.kr/). The red dot represents Typhoon, blue dots are tropical storm. The blue shaded color represents the area of which wind speed is > 15m/sec.

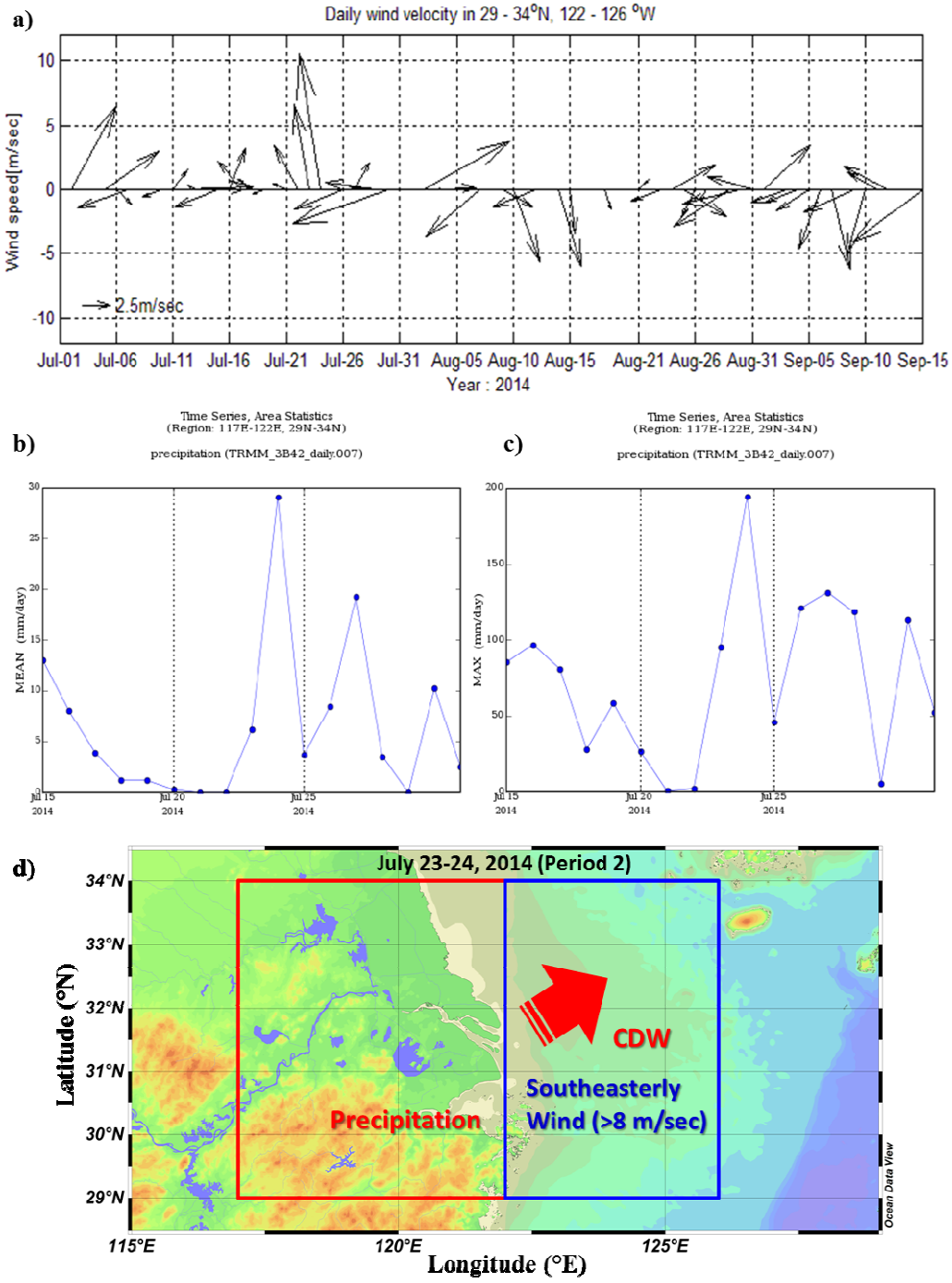

Figure 26. a) Stick diagram of wind velocity averaged near the mouth of CR (29°–34° N, 122°–126°E) from Windsat, b) Daily mean precipitation and c) Daily maximum precipitation in the Changjiang Estuary (29°–34° N, 117°–122°E) from TRMM 3B42 product (Precipitations are generated by NASA Giovanni tool at http://disc.sci.gsfc.nasa.gov/giovanni), d) Schematic diagram of the offshore advection of CDW due to precipitation and southeasterly wind (red box is area of daily precipitation, blue box is area of estimating wind velocity).

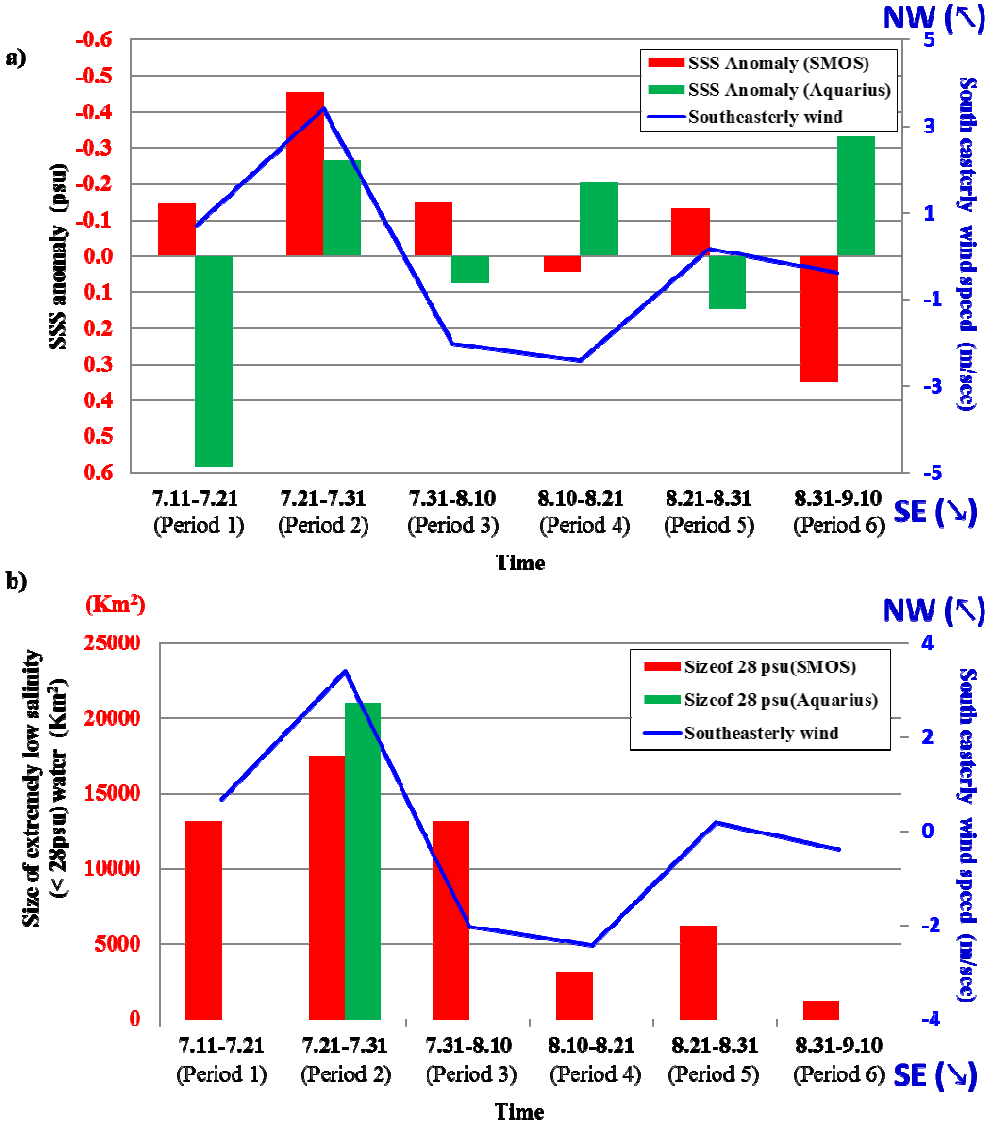

Figure 27. Diagram of southeasterly component (320° direction) of the wind speed (blue line) with a) SSS anomaly (note : positive direction is down), b) Areal size of the CDW of extremely low salinity water (< 28 psu) in the mouth of CR (29–34°N, 122–126°E, see blue box in Figure 26d).

The high temporal resolution of SMOS (3 days) also is beneficial in capturing the patches of CDW. In contrast, Aquarius relied upon a single ascending pass in the ECS, with longer revisit cycle (7 days) than SMOS.

In order to prove the capability of SMOS in capturing the spatial variation of low salinity waters driven into the ECS by southeasterly winds, histograms of SSS anomaly from averaged SSS near the CR mouth (blue box in the figure 26d) during

period 1–6 was compared between Aquarius and SMOS (Figure 27). Southeasterly wind speed at 320° component was calculated from Windsat data.

As shown in the figure 27a, $SSS_{SMOSECS}$ shows negative anomaly when alongshore wind's blowing is strong (Southeasterly). In addition, the areal size of < 28 psu water varies depending on the magnitude of the southeasterly wind speed (Figure 27b) instead Aquarius only detected the low salinity water once in the period 2. Of course, positive anomalies occurring with increasing northwesterly (i.e., southeastward) wind likely shows the role of wind direction for expanding CDW (Chang & Isobe, 2003; Moon et al., 2009). Thus, $SSS_{SMOSECS}$ successfully retrieved evidence of Ekman advection of coastal low salinity water. It did so with better spatial resolution than Aquarius and it would not have been possible without the procedures developed in this dissertation for quality controlling the data. Afterward, $SSS_{SMOSECS}$ was spatially averaged to 120×120 km in order to compare with $SSS_{AQL3ECS}$ for period 1–6. As a result, relatively good agreement of SMOS with Aquarius was found (i.e., RMSE < 0.8 psu, geometric mean slope > 0.7 and the mean bias < 0.4 psu) in periods 4 and 6 (Figure 28 d, f), during which a slight amount of the extremely low salinity was observed (Figure 24 d,f). However, the large RMSE between SMOS and Aquarius during the other periods occurred probably because SMOS captures small scales of extremely low surface salinity features more frequently with higher resolution than Aquarius. This results in more negatively biased SMOS relative to Aquarius SSS, high RMSE and away from one to one slope. Consequently, despite the potential risk of RFI, SMOS showed its utility for monitoring small-scale movement of low salinity water in ECS, through using empirically modified use of flags and spatial and temporal averaging of L2 SSS.

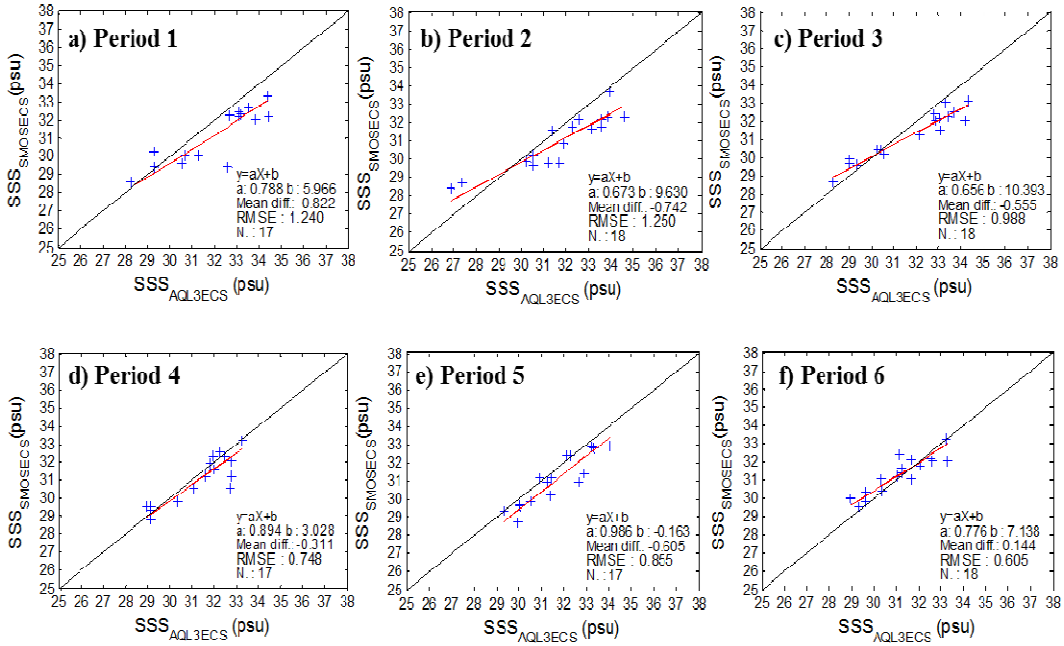

Figure 28. Comparison between collocated $SSS_{SMOSECS}$ (10 days; 120×120 km) and $SSS_{AQL3ECS}$ (7days). The collocation of SMOS is < 0.5° from Aquarius grid point. Red line represents slope equation between $SSS_{SMOSECS}$ and $SSS_{AQL3ECS}$ estimated by GM regression. Period 1–3 and 5 is when extremely low salinity (< 28 psu) is presented (see Figure 23, 24).

The historical trajectories of drifting buoys, started to the east of Jeju Island (black arrows in Figure 29a), and schematically described direction (green dashed line in Figure 29a) from previous research (Xuan et al., 2012) might imply the eastward offshore advection of detached low salinity water (red polygon close to the west coast of Jeju Island, Figure 29a) over to Jeju Island by ambient currents. Because the majority of saline water off the CR mouth is from the TWC, which flows northeastward along the coast of China, patches of CDW are advected toward Jeju Island (Chen et al., 2008; Moon et al., 2009; Naimie et al., 2001). The speed of outflowing CR plume off the river mouth was simulated to be about 10 cm/sec in the summer season (Chen et al., 2008; Naimie et al., 2001). Moving northeastward, the detached CDW is known to maintain the speed of 7–13 cm/sec to the north of Jeju Island (Lei et al., 2003).

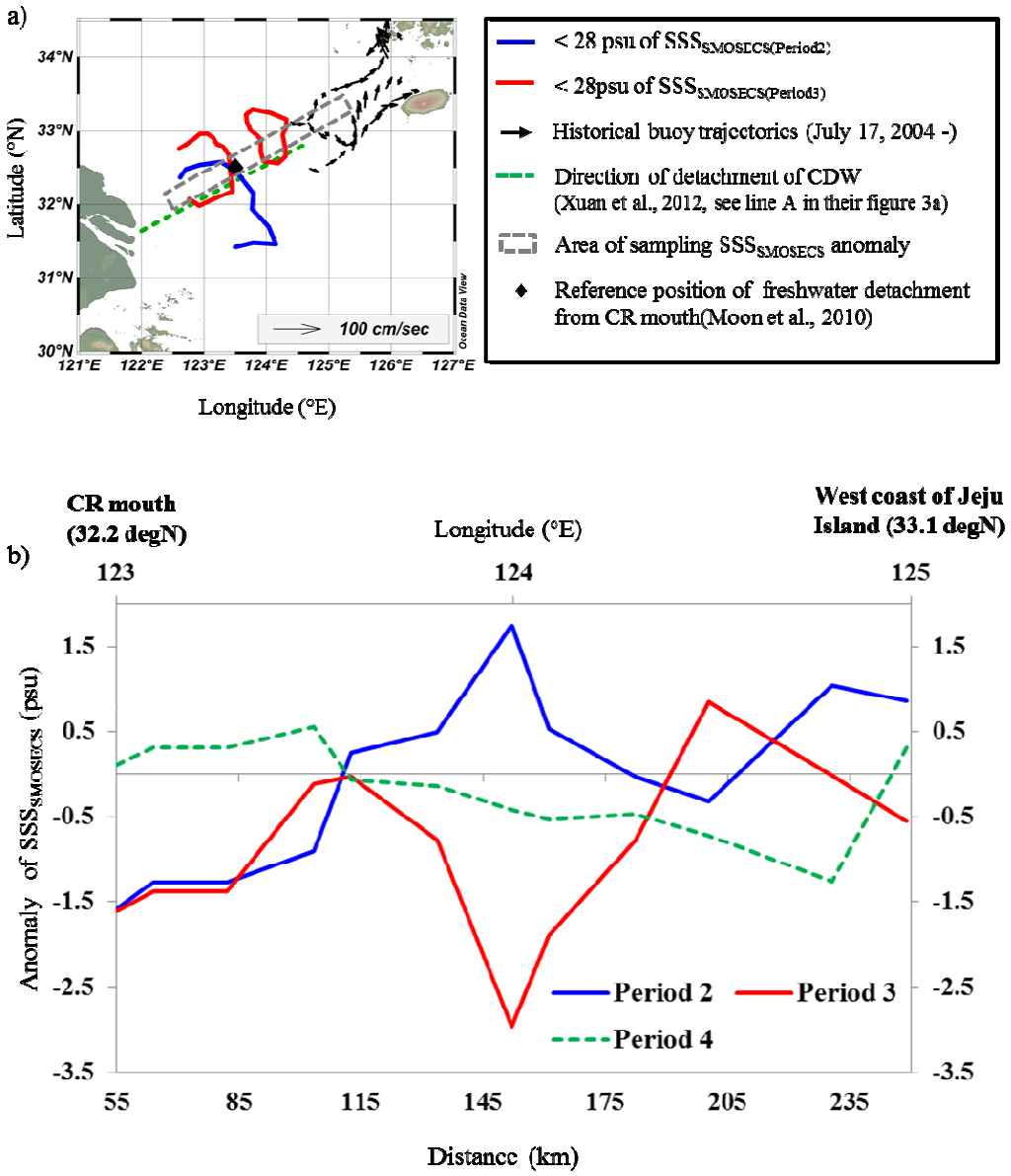

Figure 29. a) Low salinity water (< 28psu) from SMOS on period 2 (blue solid line) and period 3 (red solid line). The black arrows represent the historical trajectories of three drifting buoys, the black diamond is reference location of beginning offshore detachment of CDW, the green dashed line is reference direction of offshore detachment, gray dashed lined box is to sample anomaly of $SSS_{SMOSECS}$ for figure 27 for period 2–4. b) Anomaly of $SSS_{SMOSECS}$ (period 2–4) from CR mouth to west coast of Jeju Island in the gray dashed lined box.

It is hard to measure the speed of the low salinity patch from historical drifting buoys because they are distributed limitedly, and surface geostrophic currents from satellite altimetry is inaccurate due to shallow bottom depth (< 100 meters) and tidal

current. Additionally geostrophic currents do not have the Ekman flow. Thus, the speed of the patch was estimated by dividing the separate distance between the cores of lowest $SSS_{SMOSECS}$ anomalies (period 2 and 3, period 3 and 4) by 10 days (Figure 29b). The results of distaces moved of 80–100 km in 10 days give 9.26–11.57 cm/sec, which is similar with previous studies (10 cm/sec, Chen et al., 2008; Naimie et al., 2001 and 7–13 cm/sec, Lei et al., 2003).

Summary

It was found that there is an ongoing trend in reduction of RFI sources in the ECS since the beginning of the SMOS mission. SSS of SMOS L2 OS product was processed by developing an empirically determined set of procedures for utilizing SMOS quality control flags ('SMOSECS') in the ECS in an effort to collect enough measurements to be useful for scientific studies in the region. The conventional approach, which uses a global approach for throwing out data flagged as RFI, results in very small amounts of useable data. The empirical modification of the minimum threshold of Chi2P (0.05→0.001) combined with using outlier detection flag (Fg_ctrl_many_outlier) excluded severely contaminated measurements, as validated with comparisons with Aquarius and in situ data, and increased the amount of measurements available in the ECS. The 'SMOSECS' flag approach also minimized potential sources of RFI and land-sea contamination by removing the measurements < 100 km from the coast.

As result of testing newly processed SSS ($SSS_{SMOSECS}$) with in situ SSS, the average of temporal average (10 days) and spatial (25×25 km) SSS of the single swath showed RMSE of 1.123–1.403 psu and biases of -0.221–0.337 psu with respect to in situ SSS. Furthermore, the combination of ascending and descending passes successfully reduced the RMSE of $SSS_{SMOSECS}$ as low as 0.951 psu and also the

amount of negative bias decreased to -0.039–0.085 psu relative to using single passes.

The expansion of low salinity water (< 28 psu), which is known as “extremely low salinity”, causes damage to fisheries. It was captured by SMOS after Tropical storm Matmo made landfall in mainland China. Although Aquarius also captured the expansion of low salinity water, during the tropical storm when the wind was blowing strong southeasterly (6.72–10.74 m/sec) near the mouth of CR, its observations were much more limited. Though the detachment of the CDW was not caught by Aquarius, the small-scale movement of CDW due to wind-driven Ekman flow was captured by SMOS because of its higher temporal and spatial resolution. Except for the advection of CDW toward Jeju Island, 10 days averaged $SSS_{SMOSECS}$ (120×120 km) and 7 days averaged $SSS_{AQL3ECS}$ appeared in good agreement.

APPENDIX C

Calculation of percentage of available measurements of SMOS

Percentage of available measurements of SMOS of the grid point

$$= 100 \times \frac{Number\ of\ L2\ passes\ which\ are\ not\ flagged\ for\ the\ grid\ point}{Total\ number\ of\ passes\ of\ the\ grid\ point}$$

Regional flags "SMOSECS"

	Flags	Modified threshold
1. Regionally applied flags for ECS	Fg_ctrl_many_outlier	Applied
	Fg_ctrl_suspect_rfi	Not applied
	Fg_ctrl_chi2_P	0.001 < Chi2P < 0.95 (50 ≤ Dg_chi2_P ≤ 999)
	Fg_sc_high_wind, Fg_sc_low_wind	3 ≤ WS ≤ 10 m/sec
	Fg_sc_high_sst Fg_sc_low_sst	10 ≤ SST ≤ 30 °C
	Fg_sc_high_sss Fg_sc_low_sss	25 ≤ SSS ≤ 37 psu
	Fg_sc_land_sea_coast	100 km > from the coast (Land_Sea_Mask <= 9)
	Collecting area	±300 km from the center of the swath (Dg_af_fov > 130)
2. Not changed Flags (Threshold: see Appendix A)	Control flags: Fg_ctrl_range, Fg_ctrl_range_Acard, Fg_ctrl_sigma, Fg_ctrl_sigma_Acard, Fg_ctrl_reach_maxiter, Fg_ctrl_marq, Fg_ctrl_sunglint, Fg_ctrl_moonglint, Fg_ctrl_gal_noise, Fg_ctrl_num_meas_low, Fg_ctrl_retriev_fail Science flags: Fg_sc_TEC_gradient, Fg_sc_suspect_ice, Fg_sc_rain,	

The scripts of "SMOSECS" for BEAM VISAT software

An example of Alg.3 ("3" included in the name of the flag and parameter) of L2 OS

(The "false" below represents "not flagged")

Control_Flags_3.FG_CTRL_RANGE == false and

Control_Flags_3.FG_CTRL_RANGE_ACARD == false and

Control_Flags_3.FG_CTRL_SIGMA == false and

Control_Flags_3.FG_CTRL_SIGMA_ACARD == false and

Control_Flags_3.FG_CTRL_SUNGLINT == false and

Control_Flags_3.FG_CTRL_MOONGLINT == false and

Control_Flags_3.FG_CTRL_GAL_NOISE == false and

Control_Flags_3.FG_CTRL_REACH_MAXITER == false and

Control_Flags_3.FG_CTRL_NUM_MEAS_LOW == false and

Control_Flags_3.FG_CTRL_MANY_OUTLIERS == false and

Control_Flags_3.FG_CTRL_MARQ == false and

Control_Flags_3.FG_CTRL_RETRIEV_FAIL == false and

Control_Flags_3.FG_CTRL_POOR_GEOPHYS == false and

Science_Flags_3.FG_SC_TEC_GRADIENT == false and

Science_Flags_3.FG_SC_ICE == false and

Science_Flags_3.FG_SC_RAIN == false and

SSS3<=37 and SSS3>=25 and SST<=30 and SST>=10 and

WS<=10 and WS>=3 and Land_Sea_Mask <= 9 and

Dg_af_fov >= 130 and Dg_chi2_P_3>=50 and Dg_chi2_P_3<=999

Estimating Root Mean Square Error (RMSE)

$$RMSE = \sqrt{\frac{1}{n}\sum_{i=1}^{n}(X_i - Y_i)^2}$$

Here, X_i : SMOS SSS, Y_i : In situ SSS, n: total number of measurement

Geometric Mean Regression Method (Ricker, 1973)

The linear equation between two instrumental variables $x_i$and y_i is following

$$y_i = \alpha + \beta x_i$$

β represents the slope of geometric mean , α is intercept

The slope β is estimated as following

$$\beta = sign(S_{xy}) \times \sqrt{\frac{S_{yy}}{S_{xx}}}$$

In here,

$$S_{xy} = \frac{1}{n} \times \sum_{i=1}^{n}(x_i - \bar{x}) \times (y_i - \bar{y})$$

$$S_{xx} = \frac{1}{n} \times \sum_{i=1}^{n}(x_i - \bar{x})^2$$

$$S_{yy} = \frac{1}{n} \times \sum_{i=1}^{n}(y_i - \bar{y})^2$$

The intercept α is calculated as below

$$\alpha = \bar{y} - \beta\bar{x}$$

In the present dissertation, the GM slope was calculated based on SSS_{insitu} (or $SSS_{AQL3ECS}$) as x_i, and $SSS_{SMOSECS}$ as y_i

CHAPTER IV

SUMMARY AND CONCLUSION

During the summer monsoon in the ECS, the CDW, formed by the mixing of the CR plume, is driven offshore due to Ekman forcing by the southeasterly winds. Because the low salinity (< 28 psu) CDW causes severe damage to the fisheries industry in Jeju Island, it is advantageous to management of the fisheries to be able to monitor the advection of the CDW. Optical sensors on satellites can be used to detect CDW, but persistent cloudiness during the monsoon season precludes the use of these sensors for monitoring the turbid CDW from satellites. Clouds are transparent to microwave thermal emissions from the sea surface in the L-band, which is used to retrieve SSS, and so L-band radiometers can be used to monitor the advection of the CDW during the monsoon season. However, the many RFI sources in the region and contamination of thermal emission from land into antenna side lobes, have prevented the use of SSS data from the L-band satellites in the ECS. This dissertation focuses on developing new procedures for selecting SSS data from satellite-borne L-band radiometers (Aquarius and SMOS) that is not significantly contaminated by RFI or land based thermal L-band emissions. The methodology developed for selecting Aquarius and SMOS data allow for SSS data to be retrieved in the ECS, despite the fact that conventional procedures would yield no data. Based on the fact that there are on-going efforts to get L-band RFI sources switched off, some of these techniques may not be needed in the future.

Aquarius/SAC-D

The L3 SSS data for ascending passes compared favorably with in situ SSS when the data were limited to an area (AQL3ECS) at least 150 km from the coast. The data from descending passes had a large bias (-1.37 psu) with respect to in situ

SSS, though corresponding with the steady decrease in RFI sources over the years (as indicated by the reduction in the value for the flag indicating the probability of RFI contamination for SMOS data), the bias has decreased as well. Thus, in the future the descending pass SSS data may be useable in the ECS.

Using the ascending pass data, the monthly averaged $SSS_{AQL3ECS}$ had a statistically significance correlation with monthly P-E integrated over land (CR basin with a lag of one month) and over the ocean (ECS) with *P-values* < 0.05 showing robust one-month lagged relationship.

SMOS

SMOS SSS was processed to capture smaller spatial and temporal scales of advection of CDW in the ECS. Even though the data flag indicating the probability of RFI contamination has decreased with time, the conventional use of this flag removes too many L2 SSS measurements in the ECS. This provided the motivation for modifying the utilization of the data quality flags, through an empirical approach, to find usable SSS data in the ECS. Similar to the procedures used for the Aquarius data, a mask was used to eliminate data close to land that may be contaminated by the L-band thermal emission from the land. Since the distance from land where contamination can occur is related to the antenna aperture, and hence footprint of the measurement, the higher spatial resolution of SMOS allows for a mask having a shorter distance from land. For the SMOS data, a 100 km wide mask was used as compared to the 150 km mask used for Aquarius. Considering only land contamination, the higher spatial resolution of SMOS might have allowed use of a narrower land mask, but the 100 km mask was used to reduce the probability of RFI contamination. The modification of the threshold of Chi2P and outlier detection flags increased the percentage of available measurements. As a result, the $SSS_{SMOSECS}$ (25

km and 10 days) for combined use of ascending and descending passes showed better agreement with in situ SSS than use of a direction of ASC or DSC. The advection of low salinity CDW (< 28 psu) toward the northeast was observed when southeasterly winds prevailed over the CR mouth. Tropical storm Matmo's arrival at mainland China, bringing strong southeasterly winds (6.72–10.74 m/sec) and heavy landfall (194.7 mm/day maximum) coincided with the offshore detachment of CDW off the mouth of CR captured by SMOS. Compared with Aquarius, SMOS is better able to resolve small scale features of CDW affected by wind-driven Ekman advection. Aquarius was able to observe surface waters characteristic of CDW (< 28 psu) only once after the tropical storm event. The low spatial (150km) and temporal (7 days) resolution of Aquarius makes it more difficult to both observe and resolve developing low salinity features interacting with local wind, tide and ambient current. The temporal resolution is further reduced because only ascending passes are utilized because of the descending pass bias. It was not possible to utilize the enhanced spatial and temporal resolution of SMOS for earlier periods because the RFI contamination was too high.

In conclusion, temporal relationships between SSS in the ECS and P-E over the CR basin, and within the ECS itself, were realistically demonstrated using the Aquarius L3 product and in situ data, with both limited to a region at least 150 km from the coast. More spatially and temporally detailed information of advection of low salinity water (CDW) was observed with SMOS data by developing new procedures for utilizing data quality control flags, which were empirically demonstrated to reduce differences from in situ data, and by using a 100 km wide land mask. Using the ESA recommended procedures would have resulted in no SMOS SSS data in the ECS. SMOS successfully captured the small-scale movement of low

salinity water consistent with Ekman flow from southeasterly winds in the ECS. As valuable as the SMOS data are for resolving smaller temporal and spatial scales of SSS variability in the ECS, care must be taken in its use, because of the remaining RFI sources.

REFERENCES

Aksoy, M., & Johnson, J. T. (2013). A comparative analysis of low-level radio frequency interference in SMOS and Aquarius microwave radiometer measurements. *Geoscience and Remote Sensing, IEEE Transactions on, 51*(10), 4983-4992.

An, Q., Wu, Y., Taylor, S., & Zhao, B. (2009). Influence of the Three Gorges Project on saltwater intrusion in the Yangtze River Estuary. *Environmental geology, 56*(8), 1679-1686.

Beardsely, R.C., Limeburner, R., Yu, H., & Cannon, G. A. (1985). Discharge of the Changjiang (Yangtze River) into the East China Sea, *Continental Shelf Research*, *4*, 57–76.

Beardsley, R., Limeburner, C. R., Kim, K., & Candela, J. (1992). Lagrangian flow observations in the East China, Yellow and Japan seas. *La mer, 30*(3), 297-314.

Boutin, J., Martin, N., Yin, X., Font, J., Reul, N., & Spurgeon, P. (2012). First assessment of SMOS data over open ocean: Part II—Sea surface salinity. *Geoscience and Remote Sensing, IEEE Transactions on, 50*(5), 1662-1675.

Boutin, J., Martin, N., Reverdin, G., Yin, X., & Gaillard, F. (2013). Sea surface freshening inferred from SMOS and ARGO salinity: Impact of rain. *Ocean Science, 9,* 183-192

Burrage, D.M., Miller, J.L., Johnson, D., Wesson J., & Johnson, J.T. (2002). Observing Sea Surface Salinity in Coastal Domains Using an Airborne Surface Salinity Mapper, *Proceedings IEEE/MTS Marine Frontiers Oceans* 2002, Biloxi, MS, USA. 2014-2024.

Camps, A., Font, J., Vall-Llossera, M., Gabarró, C., Corbella, I., Duffo, N., ... Martín-Neira, M. (2004). The WISE 2000 and 2001 field experiments in support of the SMOS mission: Sea surface L-band brightness temperature observations and their application to sea surface salinity retrieval. *Geoscience and Remote Sensing, IEEE Transactions on, 42*(4), 804-823.

Chao, Y., Farrara, J. D., Schumann, G., Andreadis, K. M., & Moller, D. (2015). Sea surface salinity variability in response to the Congo river discharge. *Continental Shelf Research, 99*, 35-45.

Chen, C., Beardsley, R. C., Limeburner, R., & Kim, K. (1994). Comparison of winter and summer hydrographic observations in the Yellow and East China Seas and adjacent Kuroshio during 1986. *Continental Shelf Research, 14*(7), 909-929.

Chen, C., Xue, P., Ding, P., Beardsley, R.C., Xu, Q., Mao, X., ...Shi, M. (2008). Physical mechanisms for the offshore detachment of the Changjiang diluted water in the East China Sea. *Journal of Geophysical Research: Oceans (1978–2012)*, *113*(C2).

Chuprin, A., & Font, J. (2012). *SMOS L2 OS Product Performance Status Report*. *Technical report (SO-RP-ARG-GS-0056)*, ACRI-ST, ICM-CSIC, LOCEAN/ LATMOS, IFREMER/CLS. Retrieved from http://www.argans.co.uk/smos/ docs/deliverables/delivered/PPSR/SO-RP-ARG-GS-0056_L2OS-PPSR_v2.2_ 121130.pdf

Da-Allada, C. Y., du Penhoat, Y., Jouanno, J., Alory, G., & Hounkonnou, N. M. (2014). Modeled mixed-layer salinity balance in the Gulf of Guinea: Seasonal and Interannual variability. *Ocean Dynamics, 64*(12), 1783-1802.

Daganzo-Eusebio, E., Oliva, R., Kerr, Y. H., Nieto, S., Richaume, P., & Mecklenburg, S. M. (2013). SMOS radiometer in the 1400–1427-MHz passive band: Impact

of the RFI environment and approach to its mitigation and cancellation. *Geoscience and Remote Sensing, IEEE Transactions on, 51*(10), 4999-5007.

Dai, A., & Trenberth, K. E. (2002). Estimates of freshwater discharge from continents: Latitudinal and seasonal variations. *Journal of hydrometeorology, 3*(6), 660-687.

Dai, Z., Du, J., Li, J., Li, W., & Chen, J. (2008). Runoff characteristics of the Changjiang River during 2006: Effect of extreme drought and the impounding of the Three Gorges Dam. *Geophysical Research Letters, 35*, 7406.

Dai, Z., Chu, A., Stive, M., Zhang, X., & Yan, H. (2011). Unusual salinity conditions in the Yangtze Estuary in 2006: Impacts of an extreme drought or of the Three Gorges Dam?. *AMBIO, 40*(5), 496-505.

Debye, P.(1929). *Polar Molecules.* New York: Reinhold Publishing Company.

Delcroix, T., & Murtugudde, R. (2002). Sea surface salinity changes in the East China Sea during 1997–2001: Influence of the Yangtze River. *Journal of Geophysical Research: Oceans (1978–2012), 107*(C12), SRF-9.

Dinnat, E. P., Boutin, J., Caudal, G., & Etcheto, J. (2003). Issues concerning the sea emissivity modeling at L band for retrieving surface salinity. *Radio Science, 38*(4).

Drinkwater, M., McMullan, K., Marti, J., Brown, M., Martin-Neiral, M., Rits, W., ... Berger, M. (2009). Star in the sky. The SMOS payload: MIRAS. *Esa Bulletin-European Space Agency, (137)*, 16-21.

Droppleman, J. D., Mennella, R. A., & Evans, D. E.(1970). An airborne measurement of the salinity variations of the Mississippi River outflow. *Journal of Geophysical Research*, *75*(30), 5909-5913.

Durden, S., & Vesecky, J. (1985). A physical radar cross-section model for a wind-

driven sea with swell. *IEEE journal of oceanic engineering, 10*(4)*,* 445-451.

Entekhabi, D., Njoku, E. G., O'Neill, P. E., Kellogg, K. H., Crow, W. T., Edelstein, W. N., ...Van Zyl, J. (2010). The soil moisture active passive (SMAP) mission. *Proceedings of the IEEE, 98*(5), 704-716.

Entekhabi, D., Yueh, S., O'Neill, P., Kellogg, K.H., Allen, A., Bindlish., R., … West, R. (2014). *SMAP Handbook*. JPL Publication, JPL 400, 1567.

Fang, G., Zhao, B., & Zhu, Y. (1991). Water Volume Transport Through the Taiwan Strait and the Continental Skelf of the East China Sea Measured with Current Meters. *Elsevier oceanography series, 54*, 345-358.

Ferreira, V. G., Gong, Z., He, X., Zhang, Y., & Andam-Akorful, S. A. (2013). Estimating Total Discharge in the Yangtze River Basin Using Satellite-Based Observations. *Remote Sensing, 5*(7), 3415-3430.

Font, J., Camps, A., Borges, A., Martín-Neira, M., Boutin, J., Reul, N., ...Mecklenburg, S. (2010a). SMOS: The challenging sea surface salinity measurement from space. *Proceedings of the IEEE, 98*(5), 649-665.

Font, J., Boutin, J., Reul, N., Spurgeon, P., Ballabrera, J., Chuprin, A., ... & Zine, S. (2010b). Overview of SMOS Level 2 Ocean Salinity processing and first results. *In IGARSS* (pp. 3146-3149).

Font, J., Boutin, J., Reul, N., Spurgeon, P., Ballabrera-Poy, J., Chuprin, A., ...Delwart, S. (2013). SMOS first data analysis for sea surface salinity determination. *International Journal of Remote Sensing, 34*(9-10), 3654-3670.

Fournier, S., Reul, N., Chapron, B., & Tenerelli, J. (2012). Spatio-Temporal Coherence between Spaceborne Measurements of Salinity and Light Absorption in the Amazone Plume Region. *ESA Special Publication, 703*(10).

Fu, B. J., Wu, B. F., Lü, Y. H., Xu, Z. H., Cao, J. H., Niu, D., ...Zhou, Y. M. (2010).

Three Gorges Project: Efforts and challenges for the environment. *Progress in Physical Geography, 34*(6), 741-754.

Gabarró, C., Font, J., Camps, A., Vall-llossera, M., & Julià, A. (2004). A new empirical model of sea surface microwave emissivity for salinity remote sensing. *Geophysical Research Letters, 31*(1).

Gabarró, C., Martinez, J., & Font, J. (2012). *Impact of the Land-Sea Contamination on SMOS retrieved salinity (Vol. 1)*. Tech. Report. SMOS BEC, Retrieved from http://www.smos-bec.icm.csic.es/sites/www.smos-bec.icm.csic.es/files/archives/SMOS_docs/Technical_Notes/BEC-TN.2012.04.pdf.

Gao, B., Yang, D., & Yang, H. (2013). Impact of the Three Gorges Dam on flow regime in the middle and lower Yangtze River. *Quaternary International, 304,* 43-50.

Gimeno, L., Stohl, A., Trigo, R. M., Dominguez, F., Yoshimura, K., Yu, L., ... & Nieto, R. (2012). Oceanic and terrestrial sources of continental precipitation. *Reviews of Geophysics, 50*(4), RG4003.

Gierach, M. M., Vazquez-Cuervo, J., Lee, T., & Tsontos, V. M. (2013). Aquarius and SMOS detect effects of an extreme Mississippi River flooding event in the Gulf of Mexico. *Geophysical Research Letters, 40*(19), 5188-5193.

Grodsky, S. A., Reul, N., Lagerloef, G., Reverdin, G., Carton, J. A., Chapron, B., ... Kao, H. Y. (2012). Haline hurricane wake in the Amazon/Orinoco plume: AQUARIUS/SACD and SMOS observations. *Geophysical Research Letters,39*(20), L20603.

Guerrero, R. A., Piola, A. R., Fenco, H., Matano, R. P., Combes, V., Chao, Y., ... Strub, P. T. (2014). The salinity signature of the cross-shelf exchanges in the Southwestern Atlantic Ocean: Satellite observations. *Journal of Geophysical*

Research: Oceans, 119(11), 7794-7810.

Hernandez, O., Boutin, J., Kolodziejczyk, N., Reverdin, G., Martin, N., Gaillard, F., ... Vergely, J. L. (2014). SMOS salinity in the subtropical North Atlantic salinity maximum: 1. Comparison with Aquarius and in situ salinity. *Journal of Geophysical Research: Oceans, 119*(12), 8878-8896.

Hu, C., Li, D., Chen, C., Ge, J., Muller-Karger, F. E., Liu, J., ... He, M. X. (2010). On the recurrent Ulva prolifera blooms in the Yellow Sea and East China Sea. *Journal of Geophysical Research: Oceans (1978–2012)*, 115(C5).

Hyun, K. H., & Pang, I. C. (1998). Abnormally low salinity waters around Cheju Island in summer. *Bulletin of the Marine Resources Research Institute, Jeju National University , 22*, 69-78. (in Korean with English abstract).

Irisov, V. G. (1997). Small-slope expansion for thermal and reflected radiation from a rough surface. *Waves in random media, 7*(1), 1-10.

Isobe, A. (1999). On the origin of the Tsushima Warm Current and its seasonality. *Continental Shelf Research 19*, 117–133.

Johnson, J. T., & Zhang, M. (1999). Theoretical study of the small slope approximation for ocean polarimetric thermal emission*, IEEE Transactions on Geoscience and Remote Sensing, 37*(5), 2305-2316.

Kerr, Y. H., Font, J., Waldteufel, P., & Berger, M. (2000). The Soil Moisture and Ocean Salinity Mission-SMOS. *ESA Earth Observation Quarterly, 66*, 18-25.

Kerr, Y. H., Waldteufel, P., Wigneron, J. P., Delwart, S., Cabot, F., Boutin, J., ... Mecklenburg, S. (2010). The SMOS mission: New tool for monitoring key elements ofthe global water cycle. *Proceedings of the IEEE, 98*(5), 666-687.

Kil, B., Wiggert, J. D., & Howden, S. D. (2014). Evidence That an Optical Tail in the Gulf of Mexico After Tropical Cyclone Isaac was the Result of Offshore

Advection of Coastal Water. *Marine Technology Society Journal, 48*(4), 27-35.

Kim, S. B., Lee, J. H., de Matthaeis, P., Yueh, S., Hong, C. S., Lee, J. H., & Lagerloef, G. (2014). Sea surface salinity variability in the East China Sea observed by the Aquarius instrument. *Journal of Geophysical Research: Oceans, 119*(10), 7016-7028.

Klein, L., & Swift, C. (1977). An improved model for the dielectric constant of sea water at microwave frequencies. *IEEE Transactions on Antennas and Propagation, 25*(1), 104-111.

Korea Oceanographic Data Center (1984). *Newsletter No.1*. Korea Oceanographic Data Center National Fisheries Research and Development Institute (NFRDI) (in Korean). Retrieved from http://kodc.nfrdi.re.kr/.

Kudryavtsev, V. N., Makin, V. K., & Chapron, B. (1999). Coupled sea surface-atmosphere model: 2. Spectrum of short wind waves. *Journal of Geophysical Research: Oceans (1978–2012), 104*(C4), 7625-7639.

Lagerloef, G., Colomb, F. R., Le Vine, D., Wentz, F., Yueh, S., Ruf, C., ...Chao, Y. (2008). A. deCharon, G. Feldman, and C. Swift. 2008. The Aquarius/SAC-D mission: Designed to meet the salinity remote-sensing challenge. *Oceanography, 21*(1), 68-81.

Lagerloef, G., H.Y. Kao, O. Melnichenko, P. Hacker, E. Hackert, & Y. Chao (2013). *Aquarius salinity validation analysis (version 2).* Aquarius Project Document: AQ-014-PS-0016, 18. Retrieved from http://aquarius.nasa.gov/pdfs/AQ-014-PS-0016_ AquariusSalinityDataValidationAnalysis_DatasetVersion2.0.pdf.

Lerner, R. M., & Hollinger, J. P. (1977). Analysis of 1.4 GHz radiometric measurements from Skylab. *Remote Sensing of environment, 6(4)*, 251-269.

Le Vine, D. M., Lagerloef, G. S., Colomb, F. R., Yueh, S. H., & Pellerano, F. A.

(2007). Aquarius: An instrument to monitor sea surface salinity from space. *Geoscience and Remote Sensing, IEEE Transactions on, 45*(7), 2040-2050.

Le Vine, D. & Meissner, T. (2014a). *Proposal for Flags and Masks (AQ-014-PS-0006, 3 Jun 2014)*, technical report, Retrieved from ftp://podaac-ftp.jpl.nasa.gov/allData/aquarius/docs/v3/AQ-014-PS-0006_ProposalForFlags&Masks_Dataset Version3.0.pdf

Le Vine, D. M., de Matthaeis, P., Ruf, C. S., & Chen, D. D. (2014b). Aquarius RFI detection and mitigation algorithm: Assessment and examples. *Geoscience and Remote Sensing, IEEE Transactions on, 52*(8), 4574-4584.

Li, K., Zhu, C., Wu, L., & Huang, L. (2013). Problems caused by the Three Gorges Dam construction in the Yangtze River basin: a review. *Environmental Reviews, 21*(3), 127-135.

Li, M., & Rong, Z. (2012). Effects of tides on freshwater and volume transports in the Changjiang River plume. *Journal of Geophysical Research: Oceans (1978–2012)*, *117*(C6).

Lie, H. J., Cho, C. H., Lee, J. H., & Lee, S. (2003). Structure and eastward extension of the Changjiang River plume in the East China Sea, *Journal of Geophysical Research*, *108*(C3), 3077.

Liu, B. C., & Feng, L. C. (2012). An observational analysis of the relationship between wind and the expansion of the Changjiang River Diluted Water during summer. *Atmospheric and Oceanic Science Letters, 5*, 384-388.

Maisonet, V. J., Wesson, J., Burrage, D., & Howden, S. D. (2009). Measuring coastal sea-surface salinity of the Louisiana shelf from aerially observed ocean color, *OCEANS 2009, MTS/IEEE Biloxi* (pp. 1-4).

Mao, H., Gan, Z., & Lan, S. (1963). Preliminary study on the Changjiang diluted

water and its mixing natures. *Oceanologia et Limnologia Sinica, 5*(3), 183-206 (in Chinese).

Mecklenburg, S., Drusch, M., Kerr, Y. H., Font, J., Martin-Neira, M., Delwart, S., ...Crapolicchio, R. (2012). ESA's soil moisture and ocean salinity mission: Mission performance and operations. *Geoscience and Remote Sensing, IEEE Transactions on, 50*(5)*,* 1354-1366.

Meissner, T., & Wentz, F. J. (2012). The emissivity of the ocean surface between 6 and 90 GHz over a large range of wind speeds and earth incidence angles. *Geoscience and Remote Sensing, IEEE Transactions on, 50*(8), 3004-3026.

Meissner, T., Wentz, F. J., & Ricciardulli, L. (2014). The emission and scattering of L-band microwave radiation from rough ocean surfaces and wind speed measurements from the Aquarius sensor. *Journal of Geophysical Research: Oceans, 119*(9), 6499-6522.

Moon, J. H., Pang, I. C., & Yoon, J. H. (2009). Response of the Changjiang diluted water around Jeju Island to external forcings: A modeling study of 2002 and 2006. *Continental Shelf Research, 29*(13), 1549-1564.

Moon, J. H., Hirose, N., Yoon, J. H., & Pang, I. C. (2010). Offshore detachment process of the low-salinity water around Changjiang Bank in the East China Sea. *Journal of Physical Oceanography, 40*(5), 1035-1053.

Moon, J. H., Hirose, N., Pang, I. C., & Hyun, K. H. (2012). Modeling Offshore Freshwater Dispersal from the Changjiang River and Controlling Factors during Summer. *Terrestrial, Atmospheric and Oceanic Sciences, 23*(3), 247-260.

Naimie, C. E., Blain, C. A., & Lynch, D. R. (2001). Seasonal mean circulation in the Yellow Sea—a model-generated climatology. *Continental Shelf Research,*

21(6), 667-695.

NASA JPL PO.DAAC (2014). *Aquarius User Guide, Aquarius Dataset Version 3.0 (Guide Version 6.0),* JPL-D70012 AQ-010-UG-008, pp. 86. Retrieved from http://aquarius.umaine.edu/docs/AquariusUserGuide_DatasetV3.0.pdf.

Oh, K. H., Lee, J. H., Lee, S., & Pang, I. C. (2014). Intrusion of low-salinity water into the Yellow Sea Interior in 2012. *Ocean Science Journal, 49*(4), 343-356.

Oliva, R., Daganzo, E., Kerr, Y. H., Mecklenburg, S., Nieto, S., Richaume, P., & C., Gruhier (2012). SMOS radio frequency interference scenario: Status and actions taken to improve the RFI environment in the 1400–1427-MHz passive band. *Geoscience and Remote Sensing, IEEE Transactions on*, *50*(5), 1427-1439.

Oliva, R., Daganzo, E., Soldo, Y., Kerr, Y., Cabot, F., Richaume, P., ...Lopes, G.(2014). Status of RFI in the 1400–1427 MHz passive band: The SMOS perspective. *In General Assembly and Scientific Symposium (URSI GASS), 2014 XXXIth URSI* (pp. 1-4). IEEE.

Pinori, S., Crapolicchio, R., & Mecklenburg, S. (2008). Preparing the ESA-SMOS (soil moisture and ocean salinity) mission-overview of the user data products and data distribution strategy. *In Microwave Radiometry and Remote Sensing of the Environment, 2008*. MICRORAD 2008 (pp. 1-4). IEEE.

Ren, Y., Dong, Q., & He, M. (2015). Preliminary validation of SMOS sea surface salinity measurements in the South China Sea. *Chinese Journal of Oceanology and Limnology, 33*(1), 262-271.

Reul, N., & Chapron, B. (2003). A model of sea-foam thickness distribution for passive microwave remote sensing applications. *Journal of Geophysical Research: Oceans (1978–2012), 108*(C10).

Reul, N., Tenerelli, J., Boutin, J., Chapron, B., Paul, F., Brion, E., ...Archer, O. (2012). Overview of the first SMOS sea surface salinity products. Part I: Quality assessment for the second half of 2010. *Geoscience and Remote Sensing, IEEE Transactions on, 50*(5), 1636-1647.

Reul, N., Fournier, S., Boutin, J., Hernandez, O., Maes, C., Chapron, B., ...Delwart, S. (2014a). Sea surface salinity observations from space with the SMOS satellite: a new means to monitor the marine branch of the water cycle. *Surveys in Geophysics, 35*(3), 681-722.

Reul, N., Quilfen, Y., Chapron, B., Fournier, S., Kudryavtsev, V., & Sabia, R.(2014b). Multisensor observations of the Amazon-Orinoco river plume interactions with hurricanes. *Journal of Geophysical Research: Oceans, 119*(12), 8271-8295.

Ricker, W. E. (1973). Linear regressions in fishery research. *Journal of the Fisheries Board of Canada, 30*(3), 409-434.

Riedl, M. J. (2001). *Optical design fundamentals for infrared systems (Vol. 48)*. SPIE press.

Rodell, M., Beaudoing, H.K., & NASA/GSFC/HSL (2007). *GLDAS CLM Land Surface Model L4 Monthly 1.0 x 1.0 degree,version 001*, Greenbelt, Maryland, USA:Goddard Earth Sciences Data and Information Services Center (GES DISC), Data retrieved from http://disc.sci.gsfc.nasa.gov/datacollection/ GLDAS_CLM10_M_V001.html.

Schlitzer, R. (2002). Interactive analysis and visualization of geoscience data with Ocean Data View. *Computers & geosciences, 28*, 1211-1218. ODV Software retrieved from http://odv.awi.de/.

Shen, L., Xu, H., Guo, X., & Wu, P. (2012). Oceanography of Skeletonema costatum

harmful algal blooms in the East China Sea using MODIS and QuickSCAT satellite data. *Journal of Applied Remote Sensing, 6*(1)*,* 063529-1.

Shim, J. S., Lee, D. Y., Kim, S. J., Min, I. K., & Jeong, J. Y. (2009). Application of a large ocean observation buoy in the middle area of the Yellow Sea. *Ocean and Polar Research, 31*(4)*,* 401-414.

SMOS TEAM. (2008). *SMOS L2 OS Algorithm Theoretical Baseline Document*. Technical report (SO-TN-ARG-GS-0007), ICM-CSIC, LOCEAN/LATMOS, IFREMER. Retrieved from https://earth.esa.int/web/guest/-/smos-l2-os-algorithm-theoretical-baseline-document.

Suh, H. L., Cho, Y. K., Soh, H. Y., & Kim, D. H. (1999). The 1996 mass mortality of macrobenthic animals in Cheju Island: A possible role of physical oceanographic factor. *Korean Journal of Environmental Biology, 17*(2), 175-182 (in Korean with English abstract).

Swift, C. T., & McIntosh, R.E. (1983). Considerations for microwave remote sensing of ocean-surface salinity. *Geoscience and Remote Sensing, IEEE Transactions on, 4*, 480- 491.

Tang, W., Yueh, S. H., Fore, A. G., Hayashi, A., Lee, T., & Lagerloef, G. (2014). Uncertainty of Aquarius sea surface salinity retrieved under rainy conditions and its implication on the water cycle study. *Journal of Geophysical Research: Oceans, 119*(8), 4821-4839.

Teague, W. J., Jacobs, G. A., Ko, D. S., Tang, T. Y., Chang, K. I., & Suk, M. S. (2003). Connectivity of the Taiwan, Cheju, and Korea straits. *Continental Shelf Research, 23*(1), 63-77.

Tzortzi, E., Josey, S. A., Srokosz, M., & Gommenginger, C. (2013). Tropical Atlantic salinity variability: New insights from SMOS. *Geophysical Research Letters,*

40(10), 2143-2147.

UNESCO (1981). *The Practical Salinity Scale 1978 and the International Equation of State of Seawater 1980.* 10th report of the Joint Panel on Oceanographic Tables and Standards. UNESCO Technical Papers in Marine Science 36, 25.

Wang, Z., Tong, X., & Lu, H. (2014). New sea surface salinity retrieval methods based on SMOS data. *International Journal of Remote Sensing, 35*(11-12), 4371-4382.

Wentz, F. J. (2005). *The effect of clouds and rain on Aquarius salinity retrieval*. Remote Sens. Syst. Tech. Memo, 3031805. Retrieved from http://images. remss.com/papers/aquarius/rain_effect_on_salinity.pdf.

Wesson, J.C, Burrage, D.M., Maisonet, V.J., Osburn, C., Howden, S.D., & Chen, X. (2008). Aircraft and in-situ salinity and ocean color measurement and comparison in the Gulf of Mexico. *Geoscience and Remote Sensing Symposium* 2008*, IGARSS 2008. IEEE International, 4,* 383-386.

Wu, H., Zhu, J., Shen, J., & Wang, H. (2011). Tidal modulation on the Changjiang River plume in summer. *Journal of Geophysical Research: Oceans (1978–2012), 116*(C8).

Xu, K., & Milliman, J. D. (2009). Seasonal variations of sediment discharge from theYangtze River before and after impoundment of the Three Gorges Dam. *Geomorphology, 104*(3), 276-283.

Xuan, J. L., Huang, D., Zhou, F., Zhu, X. H., & Fan, X. (2012). The role of wind on the detachment of low salinity water in the Changjiang Estuary in summer. *Journal of Geophysical Research: Oceans (1978–2012)*, *117*(C10).

Yu, L., Jin, X., & Weller, R. A. (2008). *Multidecade Global Flux Datasets from the Objectively Analyzed Air-sea Fluxes (OAFlux) Project: Latent and sensible*

heat fluxes, ocean evaporation, and related surface meteorological variables. *OAFlux Project Technical Report (OA-2008-01)*. Woods Hole Oceanographic Institution. Massachusetts. Retrieved from http://oaflux.whoi. edu/

Yueh, S. H. (1997). Modeling of wind direction signals in polarimetric sea surface brightness temperatures. *Geoscience and Remote Sensing, IEEE Transactions on, 35*(6), 1400-1418.

Zine, S., Boutin, J., Waldteufel, P., Vergely, J. L., Pellarin, T., & Lazure, P. (2007). Issues about retrieving sea surface salinity in coastal areas from SMOS data. *Geoscience and Remote Sensing, IEEE Transactions on, 45*(7), 2061-2072.

Zine, S., Boutin, J., Font, J., Reul, N., Waldteufel, P., Gabarró, C., ...Delwart, S. (2008). Overview of the SMOS sea surface salinity prototype processor. *Geoscience and Remote Sensing, IEEE Transactions on, 46*(3), 621-645.